T-2820

Mossbauer Investigation of TiO_2 Powder Catalyzed Photoreduction

by

Joseph D. Brown

ProQuest LLC.
789 East Eisenhower Parkway
P.O. Box 1346
Ann Arbor, MI 48106 – 1346

T-2820

A thesis submitted to the Faculty and the Board of Trustees of the Colorado School of Mines in partial fulfillment of the requirements for the degree of Master of Science, Physics.

Golden, Colorado

Date 9/6, 1983

Signed: Joseph D Brown
Joseph D. Brown

Approved: D L Williamson
Dr. D. L. Williamson
Thesis Advisor

Golden, Colorado

Date 9/15, 1983

F D Schowengerdt
Dr. F. D. Schowengerdt
Head of Department of Physics

ABSTRACT

Mossbauer spectroscopy is used as a probe for monitoring the photoreduction of ferric ions by TiO_2 powders in an electrolytic solution to investigate what controls the efficiency of charge transfer in this system. The amount of reduction of Fe^{3+} to Fe^{2+} is compared with the length of illumination time at fixed intensity for a series of samples and the data are analyzed in terms of rate constants. Experiments are done with the semiconductor powders anatase, rutile, doped anatase, platinized doped anatase, and anatase with a hole acceptor added to the solution.

The rate constants reported are the first of their kind. Comparisons of the rate constants for the different powders provide support for several mechanisms thought to be important for photoreduction in a powder-electrolyte system. Anatase is more efficient at supporting reduction than is rutile. This is consistent with the fact that energetically it is easier for anatase to drive a reduction than rutile. It is also consistent with the fact that anatase has a smaller grain size than rutile. Doping decreases the efficiency of the anatase system, consistent with the idea that a barrier to electron injection exists in the particles. Plantinization increases the efficiency of reduction consistent with a known catalytic behavior. Finally, the addition

of the hole acceptor to the solution enhances the efficiency consistent with its hole scavenging properties.

TABLE OF CONTENTS

IST OF FIGURES

LIST OF TABLES

ACKNOWLEDGEMENTS

I would like to gratefully acknowledge Dr. Arthur J. Nozik of the Solar Energy Research Institute from whose idea this project sprang, and from whose budget the funding sprang. I would also like to express my thanks for his continuing support and advice throughout this project.

I would also like to thank my thesis advisor, Dr. Don L. Williamson, for hours of advice and discussion and experimental assistance without which this thesis could not have been accomplished.

Special thanks goes to my loving wife, Donna, for her patient support and care throughout the course of my graduate school experience. I must also express my thanks to her for the typing of this document.

Finally, the friendship and constant assistance of Thomas W. Guettinger, my lab partner, was sincerely appreciated. I count it a priviledge to have met him.

INTRODUCTION

Much of the physics of the p-n junction and Schottky-barrier type solar cell devices is well understood, but making these junctions involves many problems of growing doped single crystals. An easier way to produce the important depletion region in a semiconductor device is to immerse the semiconductor in an electrolytic solution. This produces a photoelectrochemical cell that can be used to either drive chemical reactions (photoelectrosynthesis) or to produce electricity (photovoltaics). A further simplification of photoelectrochemical cells is to suspend semiconductor particles in the solution. In this way, photoelectrosynthesis can be achieved in a very simple system.

While there has been work done with semiconductor powders suspended in liquid electrolytes[1-5], it has generally been of a qualitative character and little quantitative work has been reported concerning the nature of charge transfer at the semiconductor-electrolyte interface. This thesis is concerned with these charge transfer processes. It uses Mossbauer spectroscopy as a probe for monitoring the change of the charge states of iron ions in an electrolytic solution, in which semiconductor particles are suspended, as a function of time of illumination. Mossbauer spectroscopy is useful because no chemical

analysis need be done to determine the ferric/ferrous ratio and it is not affected by other species in solution. The ratio, therefore, may be determined in-situ, reducing the possibility of back oxidation of the ferrous ion.

This work involved titanium-dioxide (TiO_2) powders suspended in ferric chloride electrolyte. Both crystal forms (anatase and rutile) were studied. The effect of a catalytic metal (platinum) deposited on the TiO_2 semiconductor powder on the photooxidation or photoreduction process was also studied. The important question of what controls the efficiency of photo-induced charge transfer was examined in this work. These efficiencies were defined in terms of rate constants. A rate constant is a parameter in the rate equation and a higher rate constant under conditions of constant light intensity of concentration denotes a higher electron transfer efficiency. The rate constants measured in this study are the first of their kind for this type of system.

The first two sections of this thesis relate the basic principles involved in photoelectrochemistry and Mossbauer spectroscopy. The third section describes the experimental set-up and procedures used, as well as the difficulties involved with the Mossbauer spectroscopy of ions in ice. The fourth section describes the results of investigations

of the TiO_2 - $FeCl_3$ system. Conclusions are summarized in the final section.

I. PHOTOELECTROCHEMISTRY

When a semiconductor is immersed in an electrolytic solution the chemical potentials of the solid and liquid phases must equilibrate. This usually generates a depletion region in the semiconductor which varies in depth from 5 to 200 nanometers[6] depending on doping density, electrolyte, etc. The depletion layer is responsible for the separation of photogenerated electron-hole pairs. Another charged layer, the Helmholtz layer, typically exists in the electrolyte adjacent to the semiconductor surface. Figure 1 presents a model of the Helmholtz layer adsorbed on the surface of a metal.[7] In oxide semiconductors, the Helmholtz layer is caused by preferential adsorption of OH^- species on the semiconductor. This layer extends a few angstroms into the solution[8] and affects the band bending that develops in the semiconductor. Without the Helmholtz layer, the difference in potential an injected electron would see would simply equal the difference in the chemical potentials between the two phases. Figure 2 gives an approximate series of events describing the interface energetics.[9]

The equilibrated energy levels of this system change under intense illumination. In this case, a large number of electron-hole pairs are produced. As these pairs are separated by the electric field in the depletion layer, they

Figure 1 Two state model of the double layer

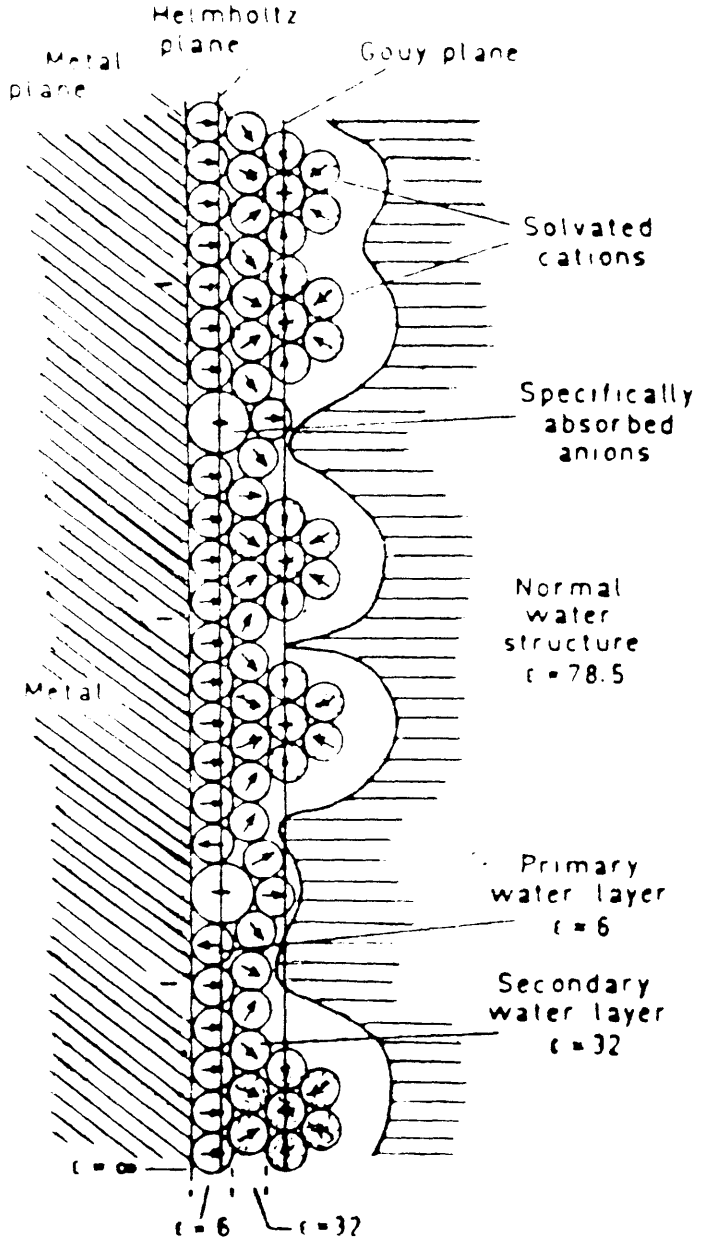

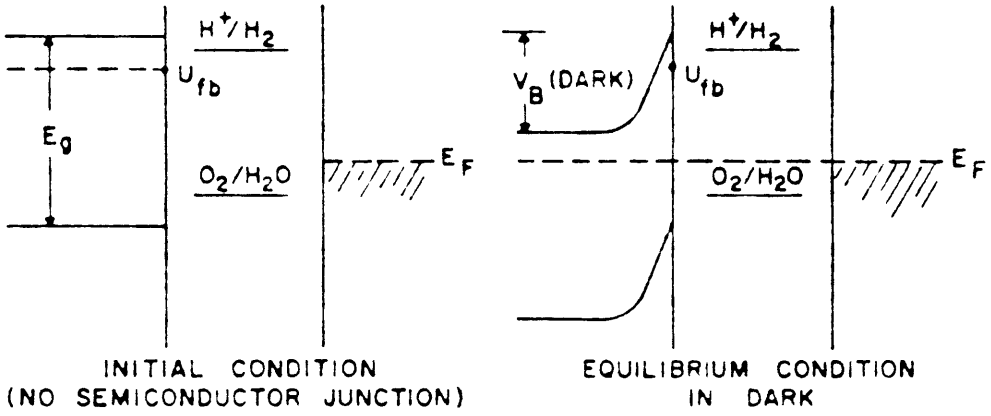

U_{fb}-flat-band potential

V_B-band bending

E_g-semiconductor band gap

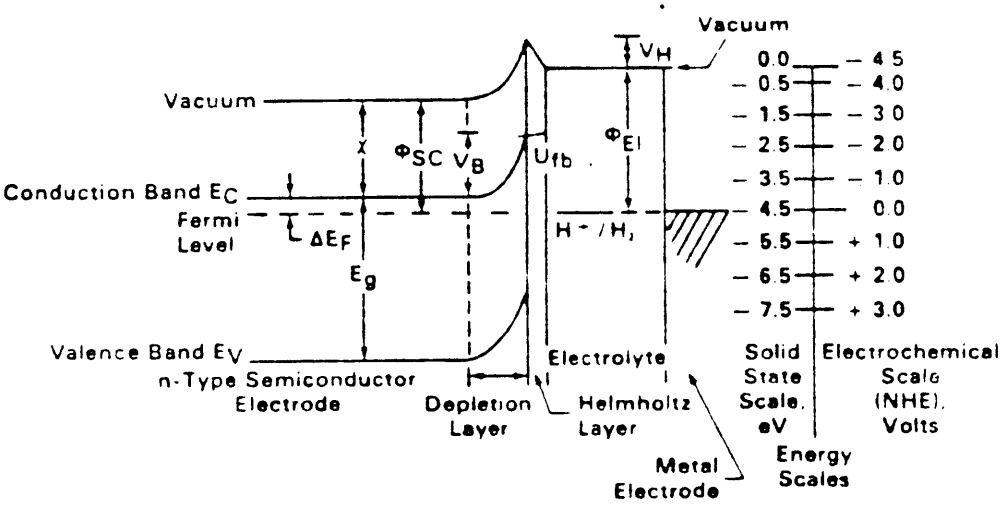

Figure 2 Energy level diagram and energy scales for semiconductor-electrolyte junctions, where the Helmholtz layer potential (V_H), work function(Φ_{sc}), and electron affinity (χ) are shown.

produce a field of their own of the opposite polarity. In short, their effect is to "unbend" the bands. The amount of decrease is labeled the photovoltage, V_{ph}. V_{ph} decreases the average field each new electron-hole pair sees, thus lowering the probability that separation occurs before electron-hole recombination. The separated electron-hole pairs are subsequently injected into the electrolyte to generate oxidation/reduction reactions at the semiconductor electrode surface. This leads to the photoelectrochemistry of the system.

The pH of the electrolyte has an effect on the relative energy levels of this system. The Helmholtz layer consists of OH^- ions adsorbed on the surface of the semiconductor. As the pH of the solution changes, the concentration of OH^- ions on the surface of the semiconductor changes via the reaction:

$$(S.C.)\ OH^- \rightarrow (S.C.) + O^{-2} + H^+$$

As this equilibrium changes the capacitance of the Helmholtz layer changes. This changes the relative positions of the energy levels in the semiconductor to those of the electrolyte. The energy levels in the latter are determined by the potential of the redox species in the electrolyte.

In addition to pH studies, investigators in this field have tried many things to increase the efficiencies of their

systems. Platinum is frequently deposited on part of the electrode surface because it is a good electron acceptor as well as an excellent catalyst for reduction. This is because it is very porous and therefore has a large surface area which can adsorb many solution ions. The addition of an electron or hole acceptor to the solution has also been studied. These species act as a sacrificial agent which are easily reduced or oxidized and permits the desired oxidation or reduction to proceed. Doped semiconductors are also frequently investigated. Normally, in an illuminated n-type semiconductor holes are injected from the semiconductor electrode, while in a p-type semiconductor electrons are injected. However, under certain conditions, for example, when the semiconductor bands are flat or the potential barrier for majority carrier injection can be overcome, electrons can be injected from illuminated n-type semiconductors and holes can be injected from p-type semiconductors. These special cases are studied in this investigation.

The photoelectrochemistry discussed so far applies equally well to many types of semiconductor-electrolyte interfaces. The interface studied here involves semiconductor powders suspended in an aqueous electrolyte. The powder was TiO_2 and the electrolyte was a 0.014 molar ferric chloride solution.

TiO_2 is of interest for several reasons. It has been extensively studied as a photoanode for the photoelectrochemical "splitting" (simultaneous reduction and oxidation) of water into H_2 and O_2. The product, H_2 could then be used as an alternate fuel. The ability of TiO_2 to split water is due to its band edge positions relative to the H^+/H_2 and H_2O/O_2 redox potentials as shown in Figure 3. With TiO_2, both photoproduced electrons and holes are injected to the solution with enough total energy to cause the aforementioned reactions to take place. As seen from this diagram, the electrons will emerge from the conduction band with enough energy to reduce any chemical species with a redox potential below the conduction band edge and the holes will emerge from the valence band with enough energy to oxidize any species with a redox potential above the conduction band edge.

A positive aspect of TiO_2 is its high stability. A stable semiconductor is one that can inject photogenerated carriers into an electrolyte, but itself will not react with the charge carriers. The latter process is called photodegredation. An example of photodegredation is:

$$CdS + 2h^+ \rightarrow Cd^{2+} + S.$$

Here the CdS electrode reacts with a valence band hole, causing oxidative degredation. This reaction can coat a CdS

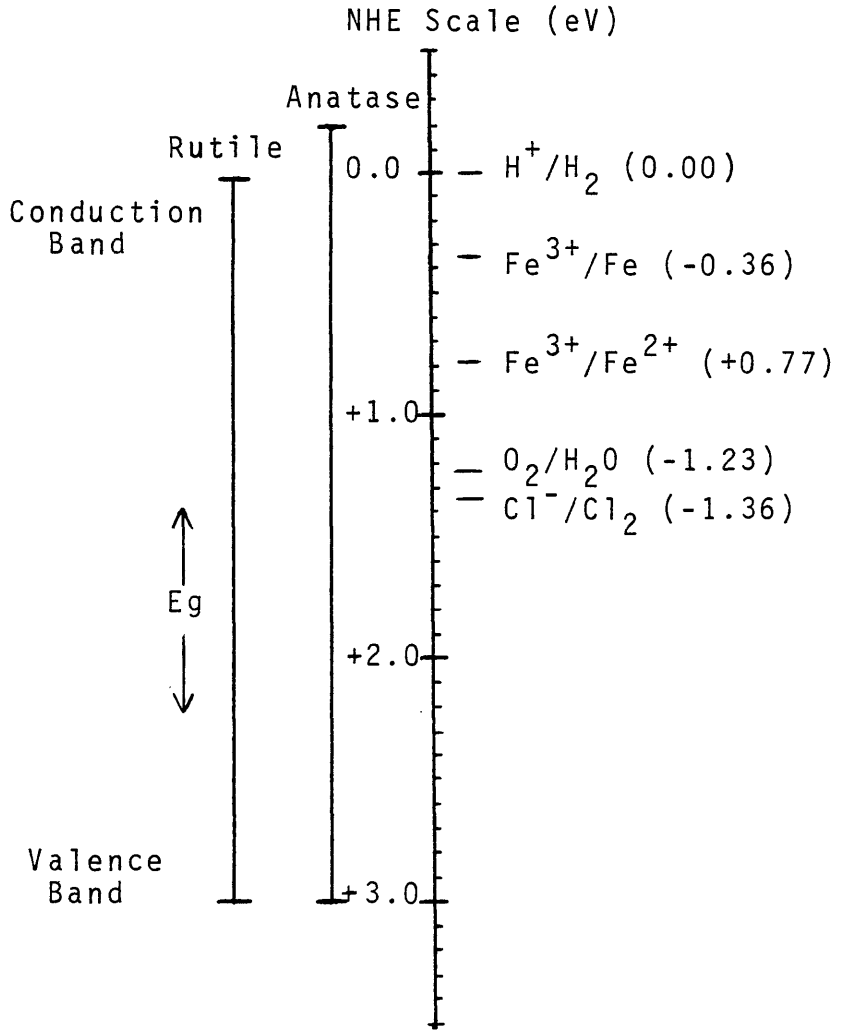

Figure 3

Position of Band gaps and pertinent redox couples.

electrode with a layer of sulfur, effectively shutting off any charge transfer process. Reactions of this type are seldom noted on TiO_2 electrodes but are very common on smaller bandgap semiconductors.

A major disadvantage of TiO_2 is its large bandgap. TiO_2 has two crystal forms, anatase with a 3.2 eV bandgap and rutile with a 3.0 eV bandgap. Since carriers can only be created by absorption of light with energy greater than the bandgap (Eg) both forms of TiO_2 can only produce a photocurrent under near-UV illumination. The sun's spectrum at the earth's surface is not very intense in the near UV, therefore, severely limiting the maximum expected overall efficiencies for TiO_2 systems.

In addition to problems that must be considered with a single-crystal electrode and metal counter-electrode system, powder semiconductors present other complications such as particle size effects, charge accumulation effects, and mixing considerations. These will be discussed in the experimental procedures section.

The electrolyte, ferric chloride, was chosen for two reasons. The first was that the position of the ferric-ferrous redox potential lies within the bandgap of TiO_2 (Fig. 3). Thus, photoexcited electrons should be able to reduce the ferric ion to the ferrous state. The second

reason was that this process could then be readily monitored using Mossbauer spectroscopy. The Mossbauer effect is more easily witnessed in ^{57}Fe than in any other nuclear species and ^{57}Fe occurs naturally with a 2 percent abundance in all iron compounds. The iron used in this electrolyte was 95% ^{57}Fe.

II. MOSSBAUER EFFECT

A. General Theory

The Mossbauer effect is recoilless gamma-ray emission and absorption by nuclei. Recoilless emission or absorption is not possible for a free nucleus, for when it emits or absorbs a gamma-ray it must gain or lose a certain amount of recoil energy, E_R. Conservation of energy requires

$$E_\gamma + E_R = E_o$$

where E_o is the nuclear transition energy. Therefore, if a gamma-ray is emitted from one nucleus, interacts with an identical nucleus and the two are initially at rest with respect to one another, the situation in Figure 4 will result. In this case, resonance florescence will most probably not take place since there is little or no line overlap. The lines are shifted by $E_R \pm E_\gamma$ where

$$E_R = P_n^2/2M; \quad E = P_\gamma c = \hbar k$$

In these equations, M is the mass of the nucleus involved, k is the magnitude of the gamma-ray wave vector, c is the velocity of light and $\hbar$ is Planck's constant divided by 2π.

The Mossbauer effect can only be observed in solids where it is possible for a gamma-ray to be emitted from a bound atam without exciting a phonon. This "zero-phonon transition"[10] has the probability, f, called the recoil-free fraction. For a one-dimensional harmonic oscillator:

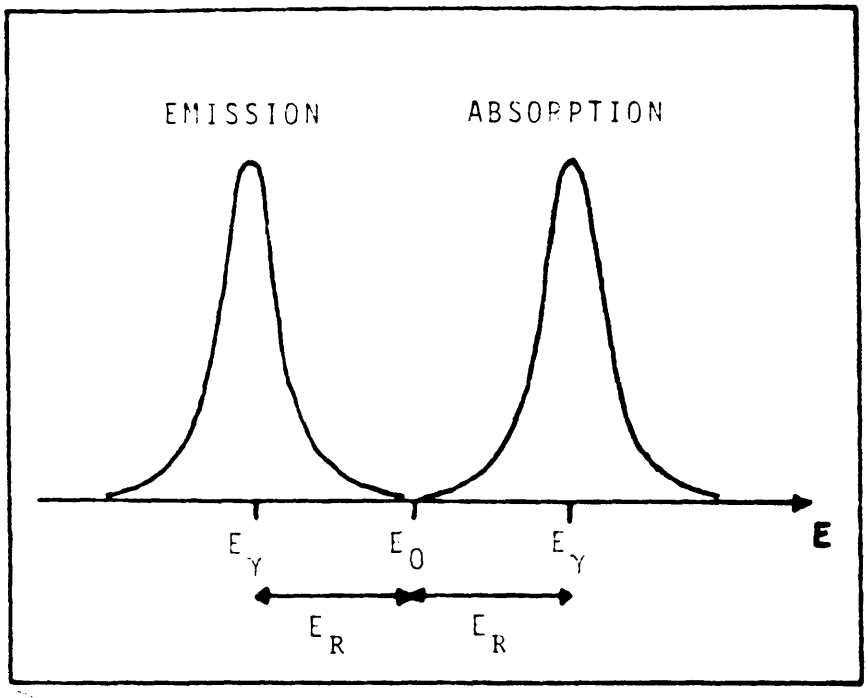

Figure 4 Emission and absorption lines shifted by E_R.

$$f = \exp(-k^2 \langle x^2 \rangle)$$

where $\langle x^2 \rangle$ is the mean-square vibrational amplitude in the x-direction

Thus, the situation can occur wherein a gamma-ray will be emitted from a nucleus in one solid and be absorbed by another nucleus in a different solid, thus causing nuclear resonance florescence. This is the Mossbauer effect. It is of interest because of the narrow natural line width of the many Mossbauer transitions. Using Heisenberg's uncertainty principal, for the 14.4 keV transition in ^{57}Fe with a 10^{-7}s lifetime, $\Delta E = 5 \times 10^{-9}$ eV and $\Gamma/E_\gamma \simeq 3 \times 10^{-13}$. This allows the experimenter to detect extremely small differences in energy levels between emitting and absorbing nuclei, and therefore makes possible the detection of all the following nuclear effects.

B. Nuclear Hyperfine Interactions

As gamma-rays are emitted from one solid and absorbed in another, there are a variety of interactions which must be considered. These hyperfine (electron-nucleon) interactions determine the number of lines and their relative positions. These absorption lines are resolved by moving the source relative to the absorber to Doppler shift the gamma-rays. The change in energy of the gamma-rays is:

$$\Delta E = \frac{v}{c} E$$

where v, the relative velocity of source and absorber, is on the order of mm/s. Therefore, the positions of the peaks are conventionally reported in mm/s rather than in energy units. The interactions of interest here are the isomer shift, quadrupole splitting, and the magnetic hyperfine interaction.

1. Isomer Shift

This electrostatic interaction arises from the change of nuclear radius between its excited and ground states, as well as the difference in electron density at the nucleus between source and absorber nuclei.

The change in energy of the gamma-ray as it goes from an excited to a ground state is then given by:

$$\delta_{E_{excited}} - \delta_{E_{gnd}} = \frac{2\pi}{5} Z e^2 |\Psi(o)|^2 (R^2_{ex} - R^2_{gnd})$$

where Ψ (o) is the total electron wave function evaluated at

R_e = o. There can be differing environments, however, from source to absorber, giving the final form for the isomer shift[11]:

$$\delta = \frac{2\pi}{5} Z e^2 \{|\Psi_a(o)|^2 - |\Psi_s(o)|^2\}\{R^2_{ex} - R^2_{gnd}\}.$$

Involved in this work are the isomer shifts of ferric and ferrous ions. In a perfectly ionic crystal Fe^{3+} has the electronic configuration $3s^2 3p^6 3d^5$ and Fe^{2+} has the configuration $3s^2 3p^6 3d^6$. The Fe-H_2O ligand is fairly polar, so these ionic configurations are acceptable for the iron ions in water. The extra d electron in the Fe^{2+} ion does not contribute directly to $\Psi(o)$ but increases the shielding of 3s electrons from the Fe^{3+} nucleus.[12] Therefore, the s electron density is higher at the nucleus of the ferric ion, and it will have a smaller isomer shift relative to the source.

Mossbauer spectra were taken of quick frozen aqueous solutions of $FeCl_2$ and $FeCl_3$. These provide an example of typical differences between Fe^{2+} and Fe^{3+} isomer shifts. The ions assumed to be trapped in ice are $Fe(H_2O)_6^{2+}$ and $Fe(H_2O)_6^{3+}$.[13] These are ferrous and ferric ions coordinated with six waters of hydration. At the temperatures involved in the experiments these ions have nearly cubic symmetry. It was generally found that the isomer shift for the ferric ion was $+0.4 \pm 0.1$ mm/sec, while for the

ferrous ion it was +1.4 ± 0.1 mm/sec.

2. Quadrupole Splitting

This interaction arises when a nuclear charge distribution deviates from spherical symmetry. This produces a tensor quantity, the quadrupole moment tensor, eQ with elements:

$$Q_{ij} = \int \rho_n x_i x_j d^3 r$$

If there exists an electric field gradient (e.f.g.) at the nucleus, its interaction with the quadrupole tensor will lift degeneracies in the nuclear levels giving rise to the observed quadrupole splitting.

Working in cartesian coordinates, both the quadrupole and e.f.g. tensors are traceless and symmetric. If the coordinate system is chosen to coincide with the principal axis of the e.f.g. tensor, the final form of the interaction Hamiltonian becomes:

$$H_E = \frac{3e^2qQ}{4I(I-1)}\{I_z^2 - I(I+1) + \tfrac{1}{2}\eta(I_+^2 - I_-^2)\}$$

where I is the nuclear spin, e is the electronic charge, I_+ and I_- are raising and lowering operators,

$$\eta = (V_{xx} - V_{yy})/V_{zz},$$

and

$$eq = V_{zz}$$

where

$$\delta^2 V/\delta i^2 = V_{ii}$$

The effect of the quadrupole interaction on nuclear states with $I \geq 3/2$ is to remove half of their $(2I + 1)$-fold degeneracy. For ^{57}Fe, which has a first excited state of $I=3/2$ and a ground state of $I=1/2$, the quadrupole interaction splits the excited state into a doublet. The combined effects of an isomer shift and quadrupole splitting are shown in Figure 5.

In this work, ferric and ferrous ions were distinguished mainly by their differing quadrupole splittings. It has been postulated that in a ferric chloride solution, the ferric ion can either be coordinated with six H_2O molecules or five H_2O molecules and a Cl^- ion to give $Fe(H_2O)_5Cl^{2+}$ which has a doublet with a quadrupole splitting of 0.25 mm/s. This is due to the distortion caused by the coordinated Cl^- ligand[15]. Only a single ferric peak could be fitted to the data in this study.

The ferrous ion, as previously mentioned, has an extra d electron whose charge distribution can easily be distorted by the slightest perturbation from cubic symmetry. This non-symmetric charge induces a large electric field gradient at the nucleus which produces typical quadrupole splittings near 3.2 mm/s.

3. Magnetic Interactions

The third electron-nucleon interaction arises from the

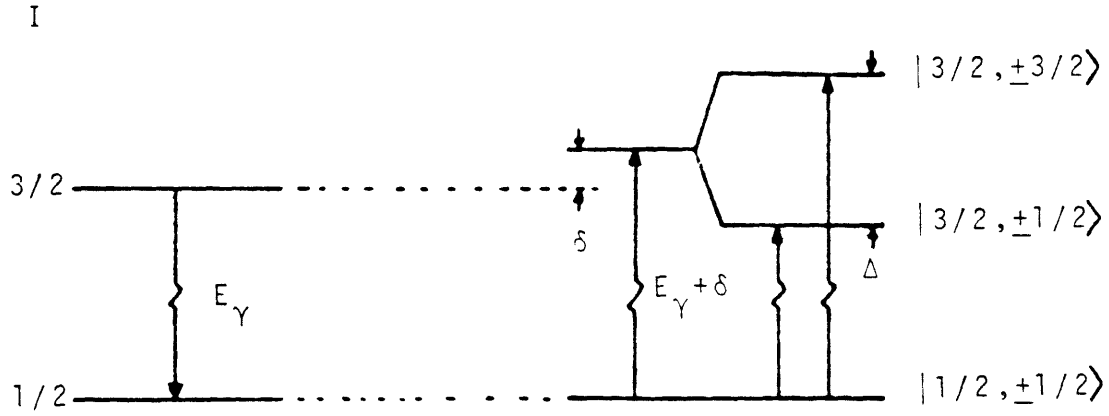

Figure 5 Isomer shift δ and quadrupole splitting Δ for ^{57}Fe.

magnetic part of the general Hamiltonian. This is further divided into two subclasses. The first is observed in ferromagnetic or antiferromagnetic systems and results from a strong internal magnetic field occuring at the nucleus. The second class occurs in paramagnetic systems with long electronic relaxation times.[16] The second class is of importance here.

In the paramagnetic system the magnetic field at the nucleus depends on the electronic relaxation time τ. If it is fast compared to $1/\omega_L$, the reciprocal of the nuclear Larmor frequency, then the magnetic field produced by the electron spins at the nucleus averages to zero and no nuclear Zeeman splitting is induced. If the relaxation time is slow compared to $1/\omega_L$ then magnetically split spectra will be observed because the nucleus no longer sees a magnetic field which averages to zero over the appropriate time interval (10^{-9}s). The intermediate case, where τ is of the order of $1/\omega_L$, will produce line broadening of the non-magnetic peaks. The fast case and the intermediate case are of interest here.

It has been postulated[17] that when water is quickly frozen, two phases can coexist, one a regular crystal lattice and one a glass-like phase. Because the solubility of ions in crystalline ice is lower than their solubility in

the glass phase, there can exist two regions of differing ion concentration. This, of course, causes different average spacings between the ions in the two phases. If the ion concentration is decreased then τ decreases because of a decrease in spin-spin interactions and a sharper paramagnetic peak will then be present.[18] This is probably the case for the crystalline phase of quick frozen ice. In the glass phase the concentration is increased, so increases and magnetic splitting or line broadening is seen. Thus, two types of Mossbauer resonance are seen for Fe^{3+}, a sharp component and a broad component. These are illustrated in Figure 6. Fe^{2+} is not affected by these considerations since it shows no paramagnetic relaxation effects.

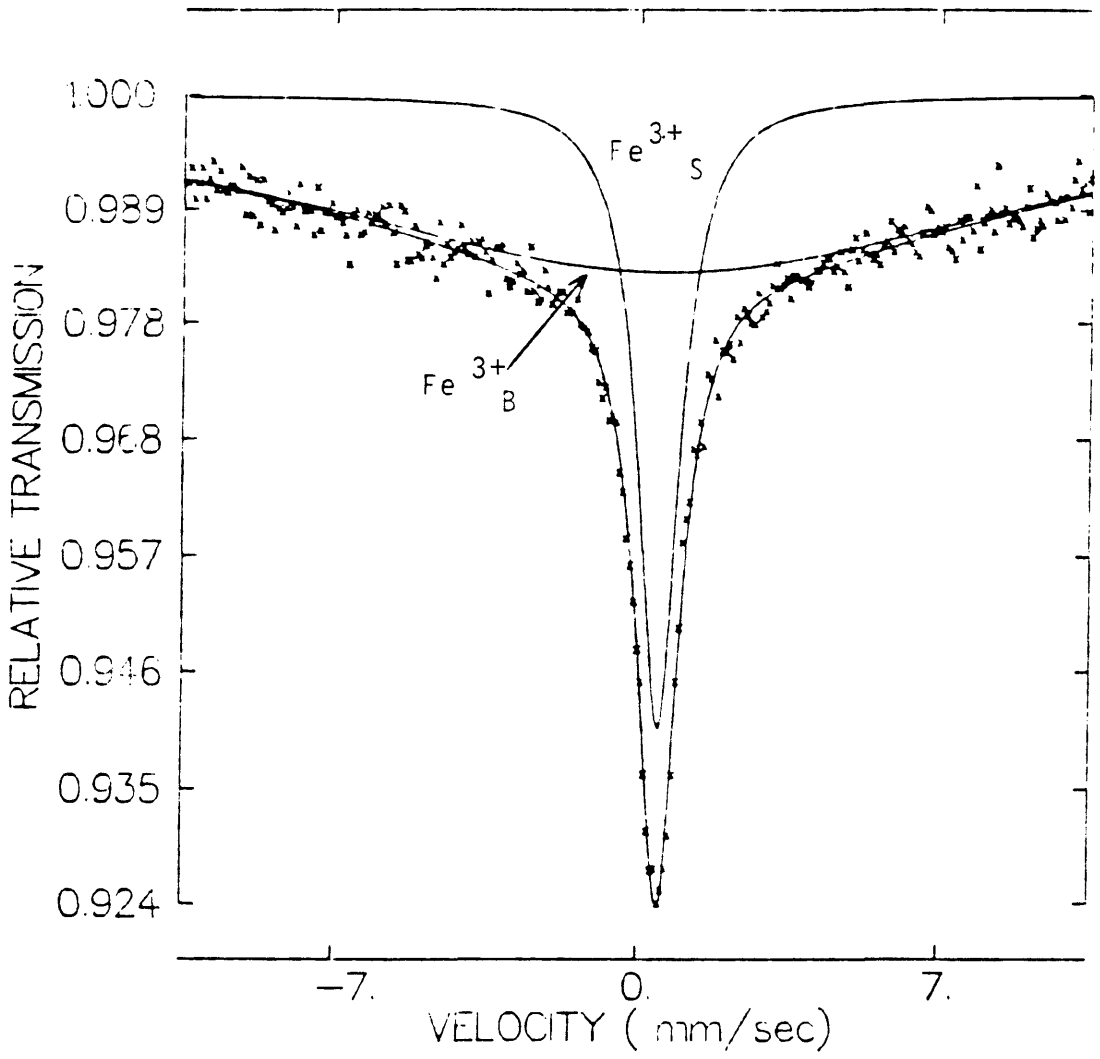

Figure 6

Mossbauer spectrum(#1561) showing both Fe^{3+} resonances.

III. APPARATUS AND EXPERIMENTAL PROCEDURES

A. Sample Preparation

The ferric chloride solution was prepared by dissolving Fe_2O_3 (95% ^{57}Fe enriched) in excess boiling 8N HCl to which H_2O was added. Frequently, some Fe^{2+} is formed in the solution, and an oxidizing agent (H_2O_2) was added to eliminate it. The final solution concentration was 0.014 molar in the Fe^{3+} ion. This roughly approximated a monolayer of Fe^{3+} ions when 20 mg of TiO_2 of average size 20 μm was suspended in 0.6 cm^3 of solution.

Both crystal forms of TiO_2, rutile and anatase, were studied. The rutile was produced by Gallard-Schlesinger and was 99.999% pure. It contained no anatase. The other variety of TiO_2 used was from MCB, was 99.9% pure, and contained 70% anatase and 30% rutile as determined by x-ray diffraction.

In addition to these powders, n-type anatase, platinized anatase, and platnized, n-type anatase were also studied. Doping to produce the n-type anatase was accomplished by heating the TiO_2 in an inert environment to approximately 1000 ^oC to induce oxygen defects in the lattice. Platinization was done according to a process documented by Bard[19] which involved photoreduction of Pt ions onto the TiO_2 particles. All of the doped and platinized

samples were supplied by Matt Radcliff of the Solar Energy Research Institute.

The samples were prepared by weighing out 20 mg of TiO_2 and putting this amount in a sample disk (see Fig. 7). A glass slip-cover 140 μm thick was then cemented on with silicone cement. The samples were illuminated through this cover-plate. After the cement dried the $FeCl_3$ solution was added by a syringe through a filler hole which was then sealed with silicone cement. The electrolyte volume of each sample disk was about 0.6 cm^3 with a 2 cm^2 frontal area.

B. Sample Illumination Procedure

The illumination geometry is shown in Figure 7. The samples were illuminated by a OSRAM 900 W lamp run by a Shoeffel 255HR 1000 W power supply. The light intensity was measured with an ORTEC thermopile and was 58.7 mw/cm^2 for each sample. Because this lamp had such an intense output in the red to infra-red region, a Nelles-Groit IR filter was kept in the beam path to eliminate possible reduction caused by IR heating of the sample. The above intensity was the value with the IR filter in place. To keep the TiO_2 particles suspended and to insure illumination of all powder the sample disks were held in a dental amalgamator and shaken while under illumination.

The possibility of spurious reduction caused by heating or some other influence was checked by shaking the sample with the lamp off as well as by heating the sample while shaking it. No Fe^{2+} was detected in any case except in the presence of illumination.

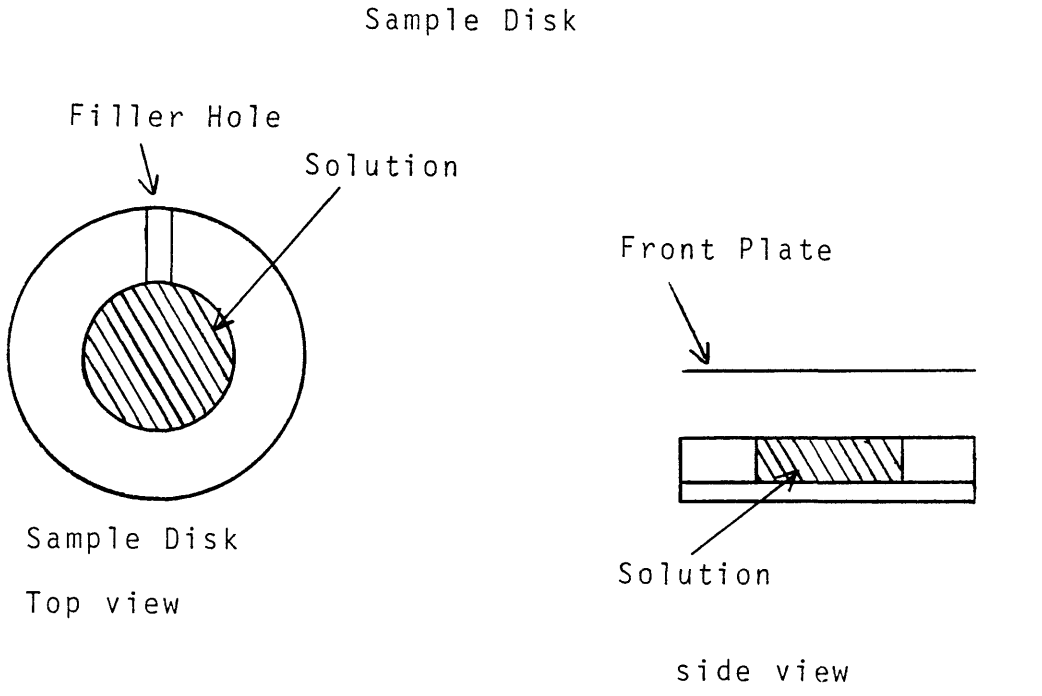

Figure 7

Illustration of Sample Disk

And Illumination Geometry

C. Freezing Procedure and Temperature Control

In preparation for the accumulation of a Mossbauer spectrum, any liquid must be converted to the solid state. The $FeCl_3$-TiO_2 suspensions were quick-frozen in their sample cells in liquid nitrogen immediately after illumination ceased. Immediate freezing was necessary to prevent any back oxidation of photoinduced Fe^{2+} to Fe^{3+}. One example of this is spectrum #1637 (Appendix II). Platinized doped anatase which had been illuminated for 45 minutes quick-frozen and measured, was then allowed to melt, refrozen and a new spectrum was taken. The first spectrum showed 10.8% Fe^{2+}, while after melting and refreezing only 4.0% Fe^{2+} was detected.

The samples were kept frozen and their temperature controlled during spectrum accumulation by a cold-finger apparatus. Temperature was controlled by adjusting the amount of dry nitrogen gas which flowed through coils immersed in liquid nitrogen then inside the cold finger, to which the sample holder was attached. The environment around the sample holder was evacuated to approximately 15 mT for each run to allow more efficient cooling. Two copper-constantan thermocouples were imbedded in the sample holder to monitor temperature during a run. It was initially found that the absolute areas of the peaks in the

spectra would change from run to run. This was attributed to the temperature history of each sample[20] and thus to phase transitions that ice had undergone.[21]

A temperature cycling procedure was found which gave the best percent effect (Peak Intensity - Background Intesity)/Background Intensity at a convenient operating temperature. A plot of percent effect of the Fe^{3+} peak versus temperature is shown for one such temperature cycle in Figure 8. The arrows in this figure show the cycling direction. Once this procedure was worked out it was used on every sample prior to accumulating a Mossbauer spectrum. It simply involved warming the sample from liquid nitrogen temperature to -80 ^{o}C then cooling to -120 ^{o}C.

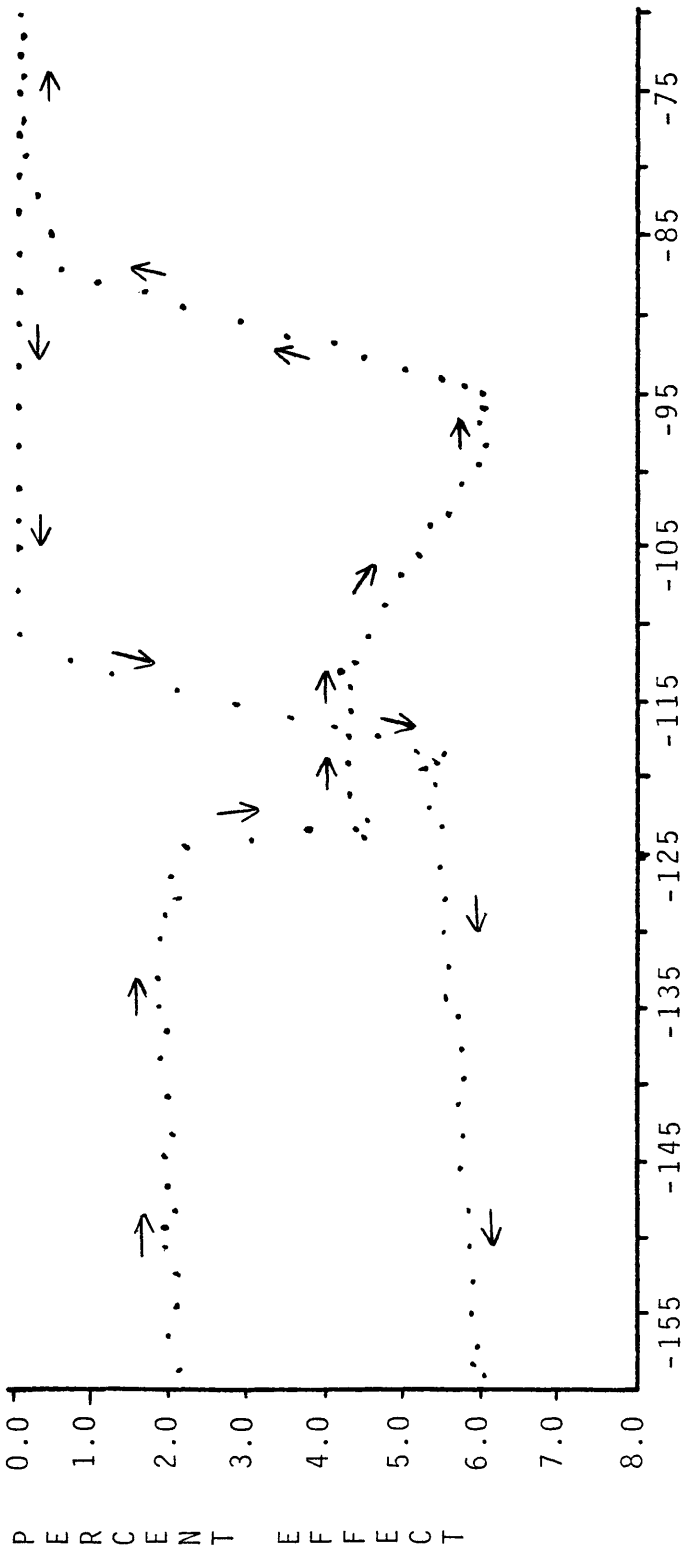

Figure 8

Plot of thermal scan results for Fe^{3+}_s peak.

D. Spectrum Accumulation

A 25mCi ^{57}Co in Rh source was used to produce the 14.4 keV Mossbauer gamma-rays. ^{57}Co (half-life 270 days) decays by electron capture to the 136.5 keV state of ^{57}Fe which then either decays directly to the ground state or in a two step process by emitting a 122 keV gamma-ray then the 14.4 keV gamma-ray. The latter happens about 91% of the time.

The energy of the 14.4 keV gamma-ray was varied slightly by the first order Doppler effect, i.e., by a relative motion of the source of the sample. This relative motion was achieved by an Elscint drive system to which the source was attached. The velocities needed for ^{57}Fe are of the order of a few mm/s. Using transmission geometry an absorption spectrum (counts versus source velocity) was then obtained and stored in 256 channels of a Tracor-Northern model 701 multichannel analyzer. The absolute velocity scale was determined by calibrating the spectrometer periodically with the well known spectrum of metallic iron.

E. Data Handling

After the spectrum accumulated, it was transferred to an Apple II computer and stored on floppy disk. It was then transferred from the Apple to a main frame computer, a DEC-10, where a superposition of Lorentzian peaks was fitted to it by a least squares method.

An important aspect of this thesis was to determine the relative amounts of Fe^{3+} to Fe^{2+} in the frozen solutions. It was assumed that the f values for Fe^{3+} and Fe^{2+} sites were the same. The amount of each species, therefore, was proportional to its peak area in the velocity spectrum.

The area of each resonance line may be calculated by the formula:

$$A_i = \frac{\pi}{2} \Gamma_i (N_\infty - N_i)/N_\infty$$

Γ refers to the peak width at half-height, N_∞ is the off-resonance counts, N_i is the on-resonance counts and the subscript i refers to the ith line in the spectrum. Computer fitting was usually done allowing the Fe^{3+} peaks to have independent intensity, position and width parameters and the Fe^{2+} peaks were fit as a quadrupole pair. Areas were then calculated for each peak and the Fe^{2+}/Fe^{3+} ratios were determined.

Two problems were encountered, however, with the spectra involving the frozen aqueous solutions of iron ions.

The first involved the positions of the lower velocity Fe^{2+} peak and the narrow Fe^{3+} peak. It was sometimes impossible to resolve the two peaks. When this occurred, the Fe^{2+}/Fe^{3+} ratio was calculated assuming a symmetric quadrupole pair for Fe^{2+} ion. The same area which the computer fit to the higher velocity Fe^{2+} peak was assigned to the lower velocity Fe^{2+} peak and was subtracted from the narrow Fe^{3+} peak to conserve total resonance area. Some anisotropy has been noted for the Fe^{2+} species in hexagonal ice [22] but the ambient ice phase was assumed to be nearly cubic because of the temperature cycling done here, so no anisotropy was expected.

The second problem involved computer fitting of the magnetically broadened Fe^{3+} peak. The program would fit this peak with a Lorentzian line of unreasonable width, sometimes twice as wide as the entire spectrum. Such a width is too wide because the maximum magnetic field at a Fe^{3+} nucleus is 550 kG which would cause resonance to appear at maximum velocities of $\pm$ 9.5 mm/sec. in a velocity spectrum. The velocity limits of a typical spectrum for this work were $\pm$ 10.5 mm/sec. The fitted area of this broadened Fe^{3+} resonance was therefore often much too large and weighted the Fe^{2+}/Fe^{3+} ratio heavily toward Fe^{3+}. A revised area for this peak had to be calculated for each spectrum by the method outlined in Appendix I. An example

of the type of spectra on which both of these corrections were done is shown in Figure 9. Another typical spectrum with larger Fe^{2+} peaks is shown in Figure 10.

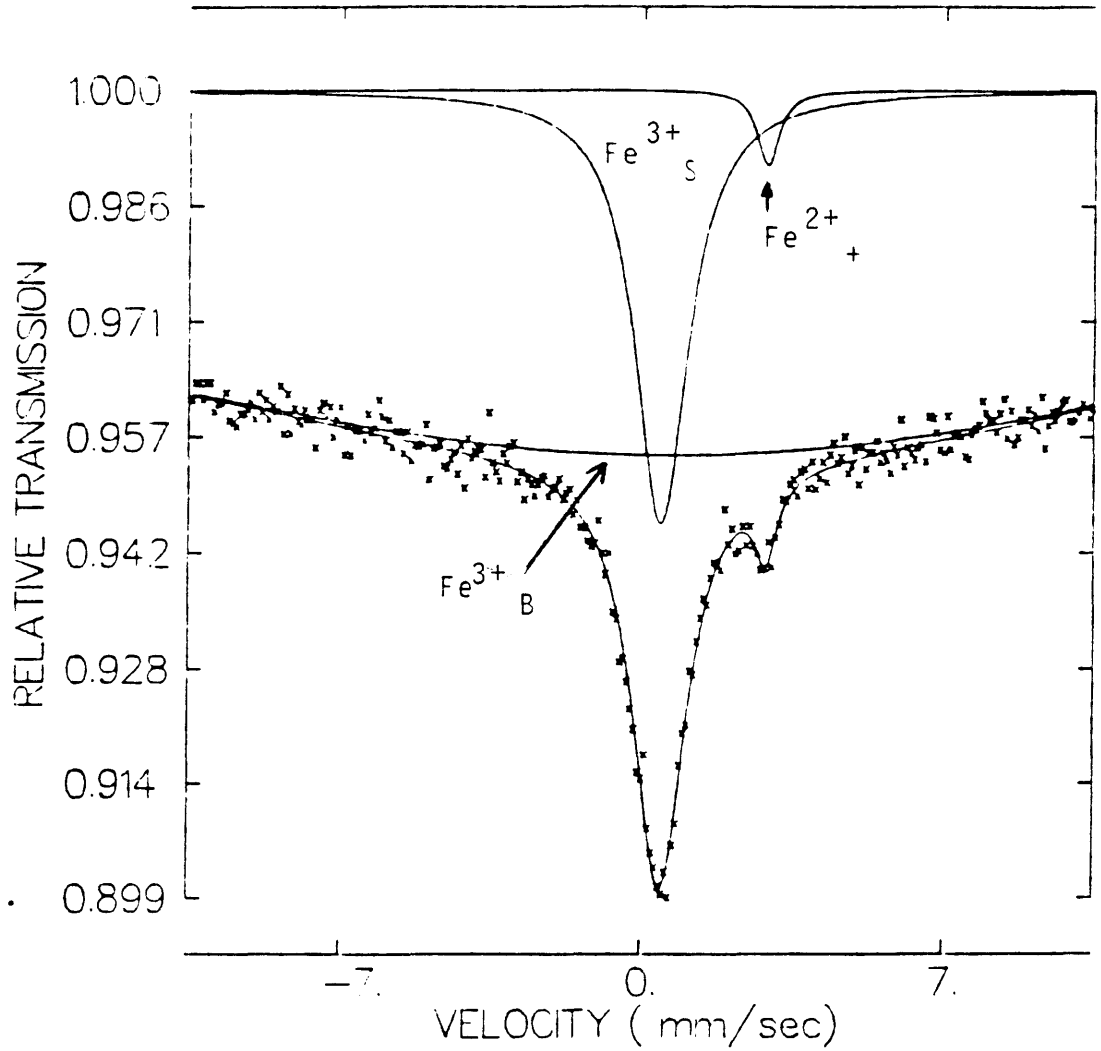

Figure 9

Mossbauer spectrum(=1572) with only one Fe^{2+} peak resolved.

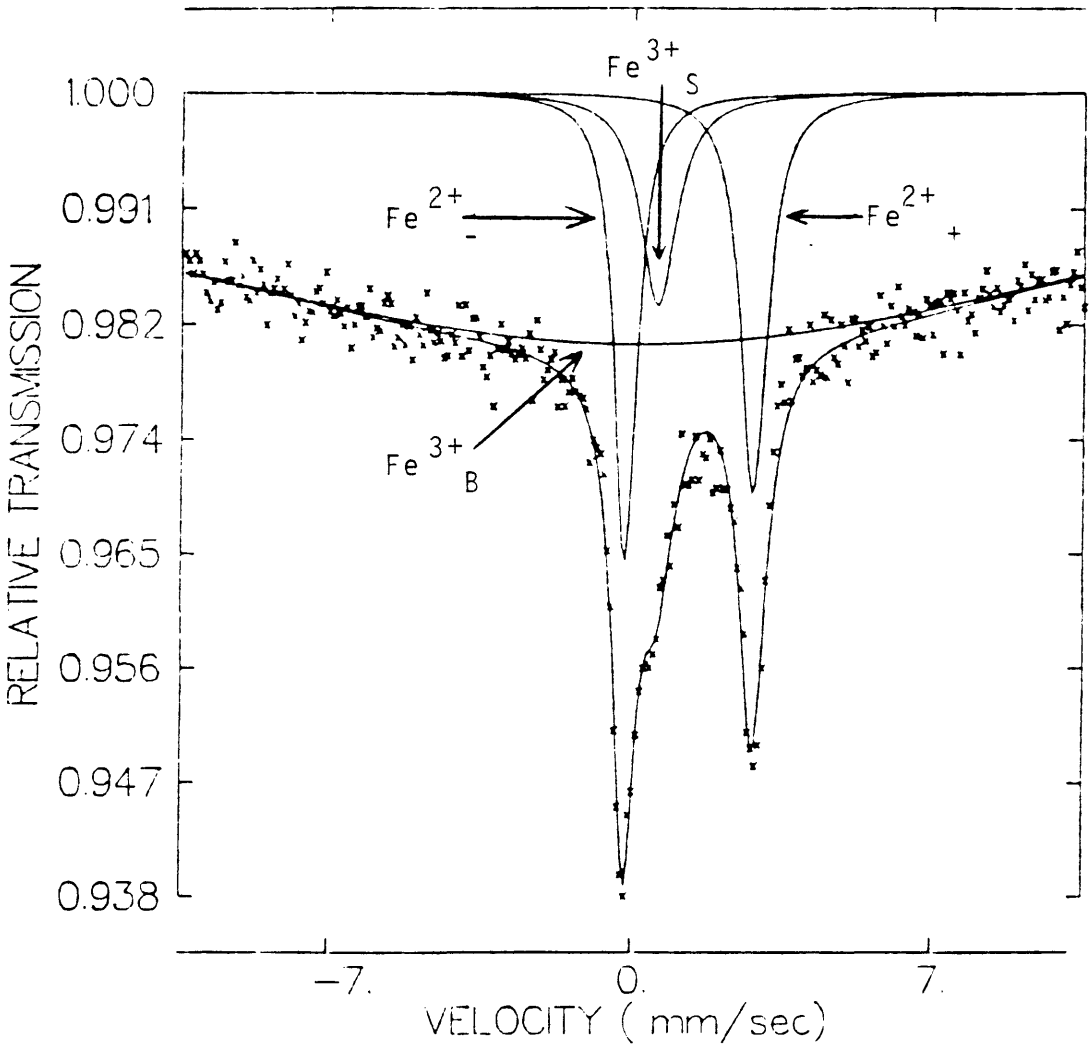

Figure 10

Mossbauer spectrum(#1715) with large amounts of Fe^{2+} evident.

IV. RESULTS AND DISCUSSION

All pertinent spectral parameters for each kinetics run are presented in Appendix II. The parameters are grouped by kinetics run, and results of special spectra are presented at the end of this appendix.

The experimental data for the five kinetics runs are presented in the following sections. The results are presented as fractional concentration of Fe^{2+}, c, versus time of illumination. c is defined to be:

$$\{Fe^{2+}\}/(\{Fe^{2+}\} + \{Fe^{3+}\})$$

where the {} denotes the area of the peaks. All illumination was done as stated in the experimental section with the sample disk approximately 2 cm from the lamp. The error bar for each point in the figures was calculated using the normal formula for the standard deviation with the values for the uncertainties in peak width and peak intensity reported from the fitting routine. Large uncertainties of some points can be traced to large uncertainties in the area of the broad Fe^{3+} component or simply to poorer statistics acquired in some spectra.

A. Kinetic Data Analysis

Electron transfer to Fe^{3+} ions as determined by c versus time of illumination, is analyzed kinetically. The reaction is,

$$Fe^{3+} + e^{-} \rightarrow Fe^{2+}$$

where for each kinetic run, an order of reaction (x) and a rate constant (k) are obtained using the rate equation:

$$dc/dt = k(1-c)^{x}$$

Chemists use the rate equation to express a relationship between the reaction rate and the concentration of the reactants. The order of reaction, x, is governed by the power to which the concentrations of the reactants are raised in the expression for the reaction rate. A reaction of the type:

$$mA + nB = C$$

has the rate equation

$$d(C)/dt=k(A)^{m}(B)^{n}$$

which is simply a statement of the Law of Mass Action[23]. This reaction is said to be of the m^{th} order with respect to the concentration of A, (A), and of the n^{th} order in (B). It should be pointed out that one cannot know the correct order of reaction simply by looking at the balanced chemical equation. This is because in some reactions, including the one in this work, many possible pathways could be involved.

All kinetics parameters such as rate constants, orders of reaction and "goodness of fit" parameters were calculated using a program entitled Fletcher-Powell. It is a common program used to obtain rate constants and related parameters from various types of kinetic data. It is a nonlinear least squares method which minimizes the sum of squared residuals, g.

$$g = \sum_i (y_{i\ obs} - y_{i\ calc})^2$$

where $y_{i\ obs}$ is the experimental point and $y_{i\ calc}$ is the calculated point for the proposed mechanism.

Breifly, the program works by the following method. The user supplies the data and the proposed equation for the mechanism of reaction; this contains the orders of reaction and rate constants. The user also supplies the equation's derivatives with respect to the parameters being searched for. The program then calculates an initial g and initial gradients. From these values the program decides how much and in what direction to increment the initial parameters. From the new parameters a new g and new gradients are calculated and the process is repeated until convergence is achieved. Convergence occurs when the g or the magnitudes of the gradients drop below a certain value, which is set by the user. The program then reports the final g, final parameters and goodness of fit parameter, which is related to g.

The objective of this work was to compare rate constants between the different sets of kinetic data to try to understand what controls charge transfer. For rate constants to be meaningfully compared they must all be calculated using the same order of reaction. The same x must be used because, for a set of data, a change in x must give a change in k. Comparing k's was easily accomplished by specifying an x and letting only k vary in the program. A small change in x was usually accompanied by very small changes in the goodness of fit parameter (see Table II). This was important because even if the best x was slightly different for each set of data, the calculated k's for the x's would only vary by a small amount.

The best fit x, the x at which rate constants for all kinetic runs were compared, was calculated from the rutile and anatase runs since these had the largest number of data points. The assumption that the same order of reaction was valid for all kinetics runs was equivalent to saying that the same mechanism of charge transfer existed for all forms of TiO_2. The details of choosing the representative x are presented in the next sub-section.

A problem was encountered in determining the uncertainty in each rate constant since the program did not provide such information. For each run the data points were

input to the program and fitted assuming a particular x. Each fit gave a k and these k's could be compared between sets of data. However, some information was needed on the precision in k based on the experimental uncertainty in each datum. Therefore, what was done was to input the top of the error bars (TEB) for each run as a data set and the bottom of the error bars (BEB) as a data set, and fit them using the best fit x. In this way some information on the uncertainties in the k's could be obtained.

B. Anatase versus Rutile

1. Results

Figure 11 presents the results for the anatase suspended in ferric chloride solution. As a check on reproduceability, certain points at the same illumination time have been repeated. They are presented as being slightly offset from each other in the case of overlap of their error bar.

One important feature is the lack of Fe^{2+} found in any solution for up to 15 minutes of illumination. This appears to be an induction period. The error bars for the points during the induction period show the minimum amount of Fe^{2+} that could be detected with the spectrum statistics.

There is no obvious explanation for the induction period for this system. It has, however, been observed in other systems[24]. Oxide semiconductors tend to specifically adsorb positive ions. This would, of course, include specific adsorption of ferric ions from the solution onto the TiO_2 surface. One would expect, once illumination began, that reduction would take place immediately. One possibility is that the photogenerated electrons are initially diverted into another reduction pathway that is necessary before the ferric reduction can proceed; however, no independent evidence for this exists.

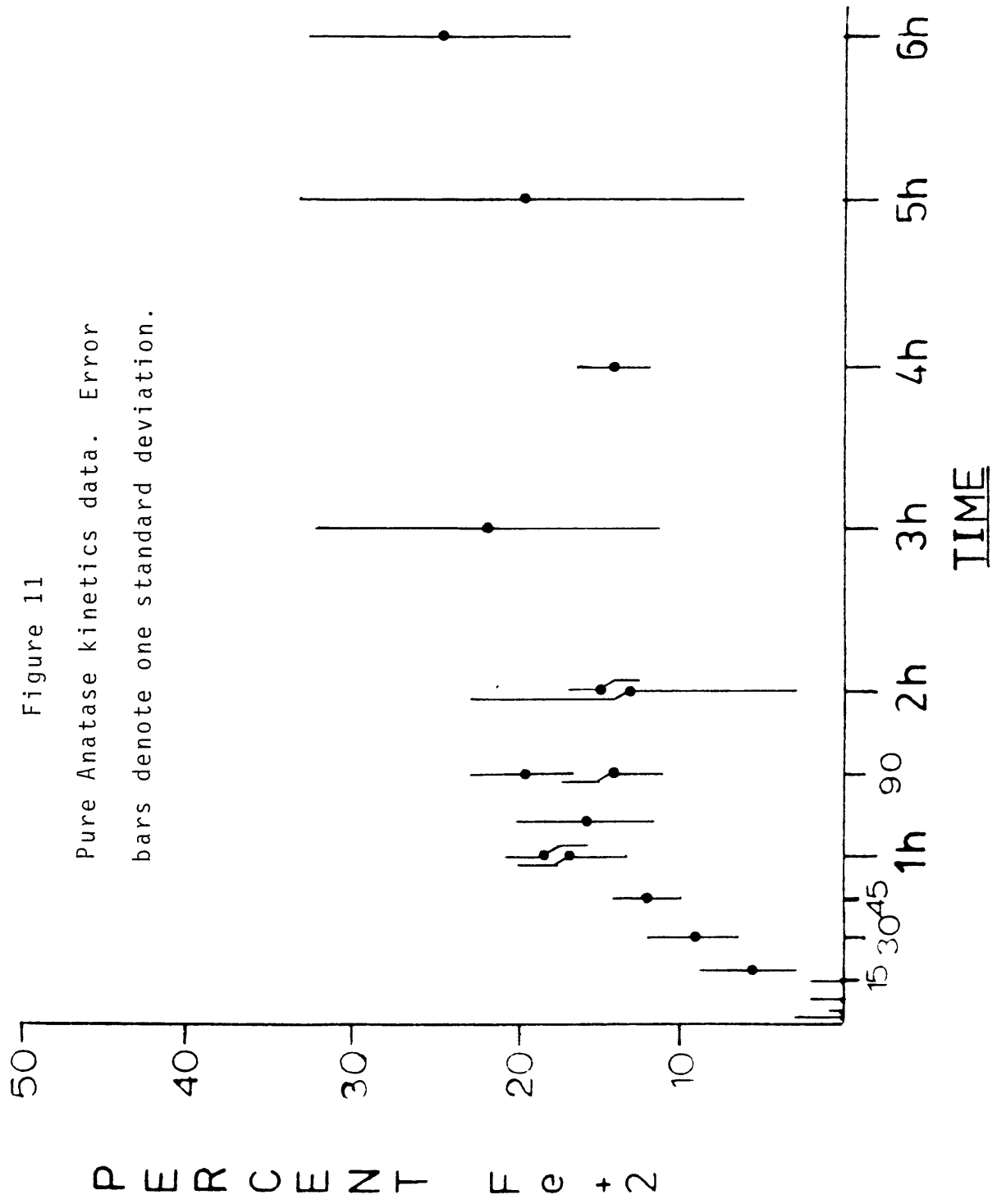

Figure 11

Pure Anatase kinetics data. Error bars denote one standard deviation.

Figure 12 shows the results for rutile. In contrast with the anatase less scatter appears in these data except at shorter times. The great disparity in c between the 25 minute point and the 30 minute point should be noted as this is not easily explained except by contamination from the filler syringe. In general, however, there is a more systematic increase in percent Fe^{2+} at longer illumination times than with the anatase. Another difference from the anatase is the apparent lack of an induction period. A significant amount of Fe^{2+} was noted after 10 minutes of illumination.

To get an estimate of the order of reaction and rate constants, both k and x were allowed to vary independently for each set of data. The induction period was taken into account by fitting the data starting at the last point where no Fe^{2+} was detected. These findings are contained in Table I. In order to get a best value for x for the combined anatase and rutile data the following procedure was used. A series of x's near the values reported in Table I were chosen. Values for k's and goodness of fit parameters, g.f.p., were then obtained for each of these x's. This is presented in Table II. To determine which x is the best value, the g.f.p.'s for each case were normalized by dividing each by the smallest number in the series. The

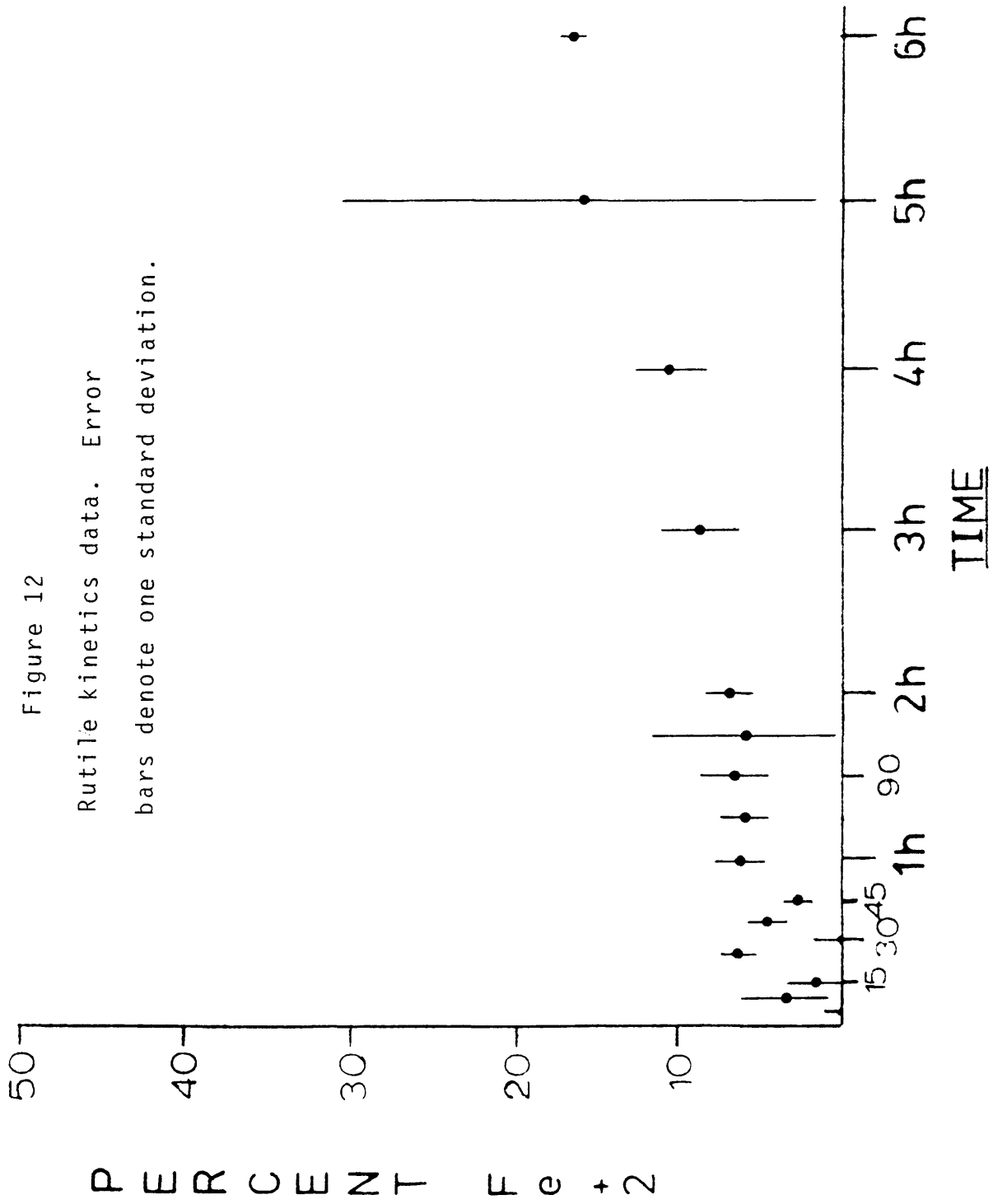

Figure 12

Rutile kinetics data. Error bars denote one standard deviation.

Table I

x and k values when both are fitted independently for anatase and rutile.

Anatase	x	k	gfp
TEB	14.51	.0022	0.222
DATA	16.25	.0010	0.203
BEB	19.32	.1091	0.229
Rutile			
TEB	10.09	.0021	0.557
DATA	6.65	.0009	1.289
BEB	18.83	.0009	0.352

Table II

Calculated k's and gfp's for specific x's.

x		13	12	11	10.5	10	9.5	9	8.5	8	7
Anatase											
TEB	k	.0144	.0120	.0100	.0091	.0083	.0076	.0069	.0063	.0057	.0047
	gfp	.029	.028	.028	.027	.027	.027	.027	.027	.028	.028
Data	k	.0073	.0063	.0054	.0050	.0047	.0043	.0040	.0037	.0034	.0029
	gfp	.020	.021	.022	.022	.023	.023	.024	.024	.024	.026
BEB	k	.0031	.0029	.0025	.0023	.0022	.0021	.0020	.0018	.0017	.0015
	gfp	.023	.024	.025	.025	.026	.026	.027	.027	.028	.029
Rutile											
TEB	k	.0028	.0025	.0023	.0022	.0021	.0020	.0019	.0018	.0017	.0016
	gfp	.017	.016	.015	.015	.015	.014	.014	.013	.013	.013
Data	k	.0014	.0013	.0012	.0012	.0012	.0011	.0011	.0011	.0010	.0009
	gfp	.004	.003	.003	.003	.003	.002	.002	.002	.002	.002
BEB	k	.0007	.0007	.0006	.0006	.0006	.0006	.0006	.0006	.0005	.0005
	gfp	.016	.015	.015	.015	.014	.014	.014	.014	.014	.014

resulting g.f.p.'s were summed for each x. These are compiled in Table III. The x with the lowest sum was assumed to be the overall best fit, and this value was determined to be x = 9.5. There is no physical explanation for the order of a reaction to be this large. The largest order typically encountered is x = 3. This large x might be caused by the system saturating with Fe^{+2} at some value much less than 100%.

It should be noted that the g.f.p.'s for the neighboring x's varied only slightly, hence this is a shallow minimum. Plots of the fits overlaying the data are presented in Figures 13 and 14. The best fit k values are

$$k(\text{anatase}) = 0.0043 \quad {}^{+0.0033}_{-0.0022}$$

$$k(\text{rutile}) = 0.0012 \quad {}^{+0.0009}_{-0.0006}$$

It was not deemed necessary to correct for the presence of 30% rutile in the anatase used in these experiments because of the uncertainties accompanying the points and the fact that the difference in their efficiencies might not be related to crystal structure. Other possibilities are indicated below.

2. Discussion

The results of the above analysis clearly show rutile has a lower overall rate constant than anatase. Although the band gap for rutile is somewhat smaller than anatase, (3.0 eV versus 3.2 eV), anatase has a more negative conduction band potential than rutile (see Figure 3). This would

Table III

Normalized gfp's for each x

x	13	12	11	10.5	10	9.5	9	8.5	8	7
Anatase										
TEB	1.07	1.04	1.04	1.00	1.00	1.00	1.00	1.00	1.04	1.04
Data	1.00	1.05	1.10	1.10	1.15	1.15	1.20	1.20	1.20	1.30
BEB	1.00	1.04	1.09	1.09	1.13	1.13	1.17	1.17	1.22	1.26
Rutile										
TEB	1.31	1.23	1.15	1.15	1.15	1.08	1.08	1.08	1.00	1.00
Data	2.00	1.50	1.00	1.00	1.00	1.00	1.00	1.00	1.00	1.00
BEB	1.14	1.07	1.07	1.07	1.00	1.00	1.00	1.00	1.00	1.00
SUM	7.52	6.93	6.45	6.41	6.41	6.36	6.45	6.45	6.46	6.60

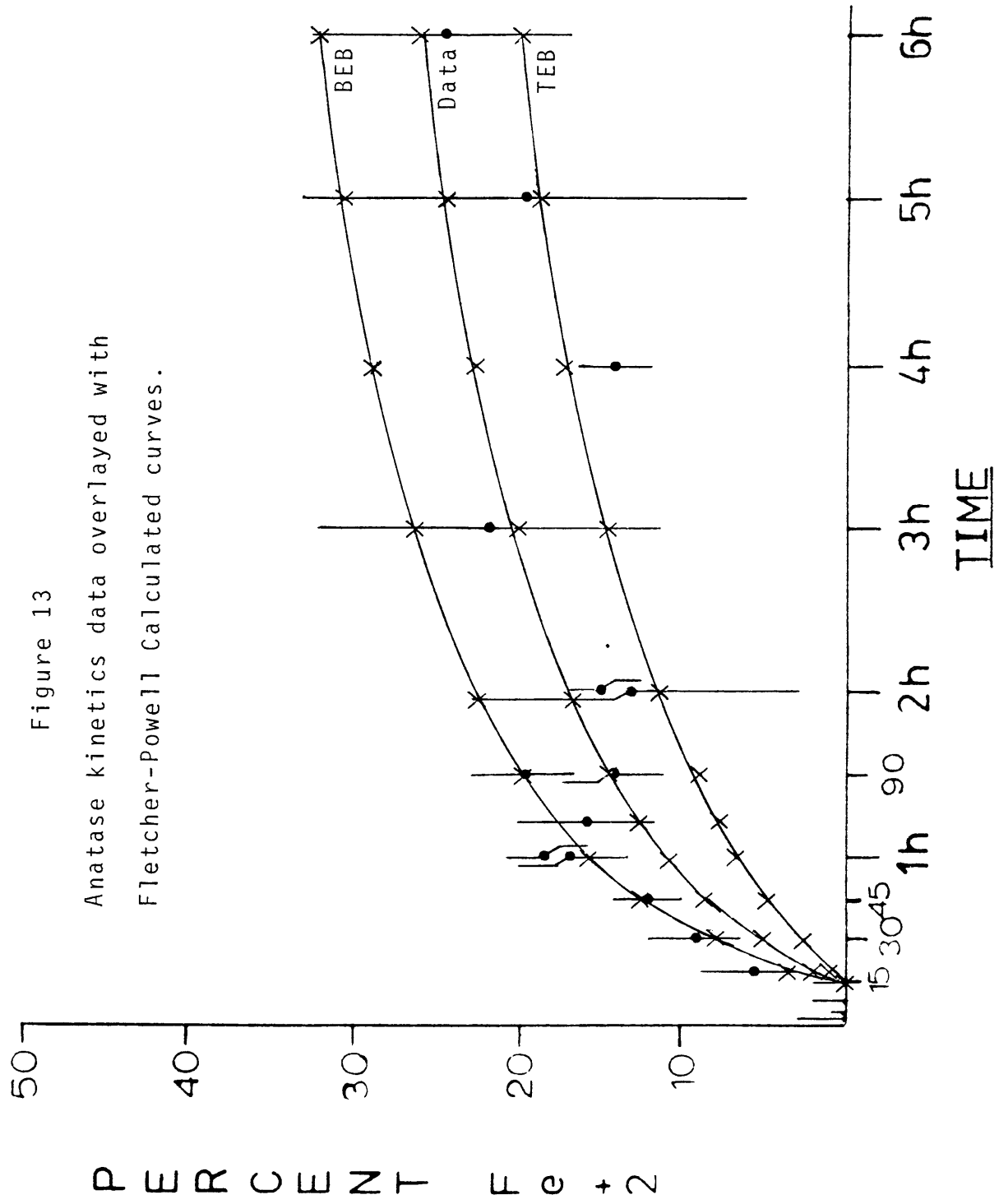

Figure 13

Anatase kinetics data overlayed with Fletcher-Powell Calculated curves.

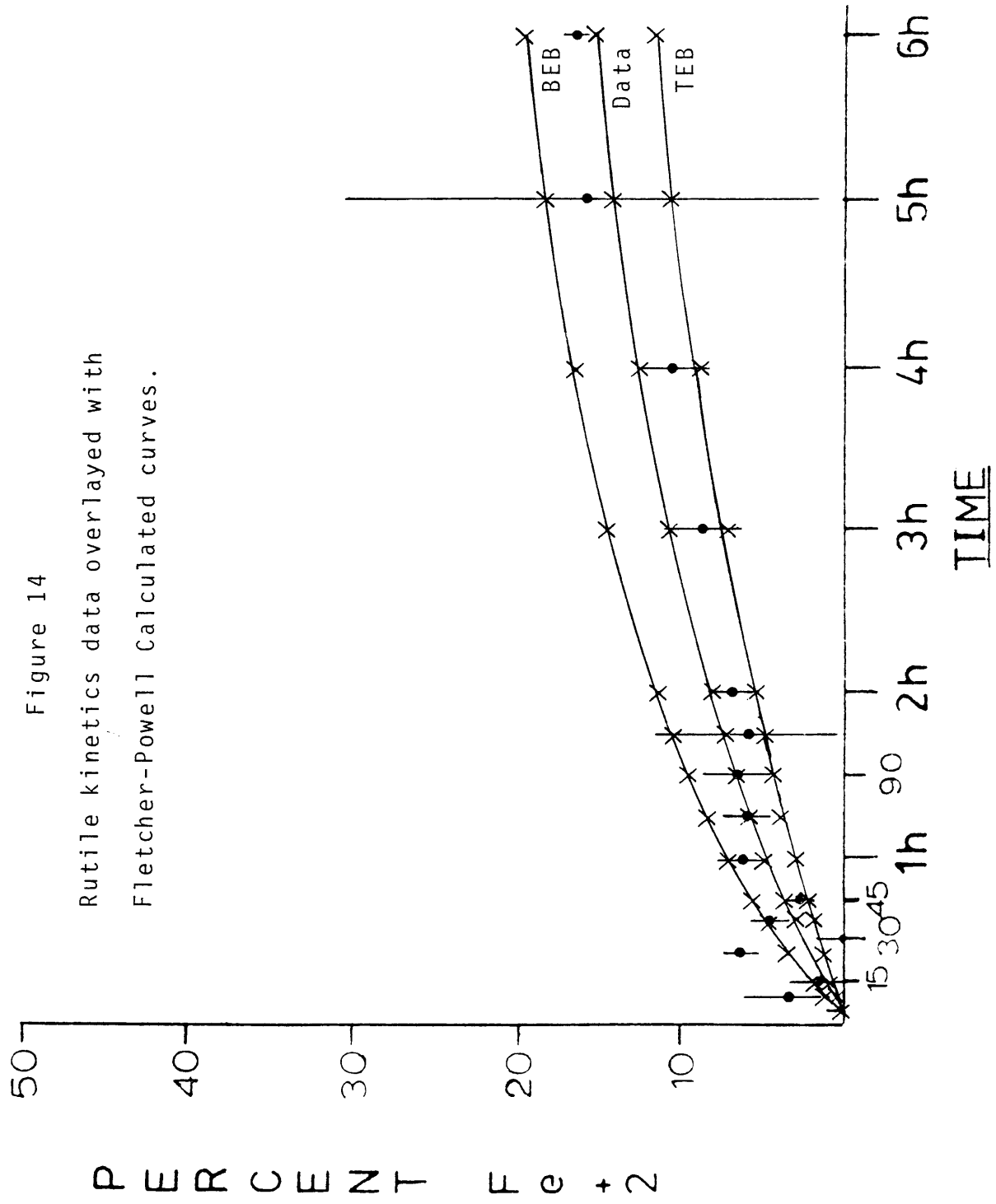

Figure 14

Rutile kinetics data overlayed with Fletcher-Powell Calculated curves.

make the driving force for the reduction greater for anatase compared to rutile. This band edge difference thus appears to be more important than the effect of the larger band gap of anatase, hence its lower quantum efficiencies.

However, another possible explanation involves consideration of the particle and grain sizes. Grains are the small single crystals which have formed together to make the larger particles. Anatase particles were all able to pass through 400 mesh sieves with an opening size of 35 microns. Only 40% of the rutile particles were able to pass. Since smaller particles have a greater surface area per unit weight, the kinetics of charge transfer should be greater for the anatase. However, reductions done with the sieved particles showed no significant change in the amount of reduction (see Table VIII).

Electron micrographs of the two TiO_2 materials indicate a difference in grain sizes. As shown in Figure 15, grain size of the anatase is much smaller, about 1 micron, than that of rutile, about 10 microns. This might explain the difference in their rate constants. Smaller grains are important because they increase the amount of surface area per unit weight of material. Therefore, smaller grains provide more area on which solution species can be adsorbed. No attempt was made to quantify the effect of grain size on

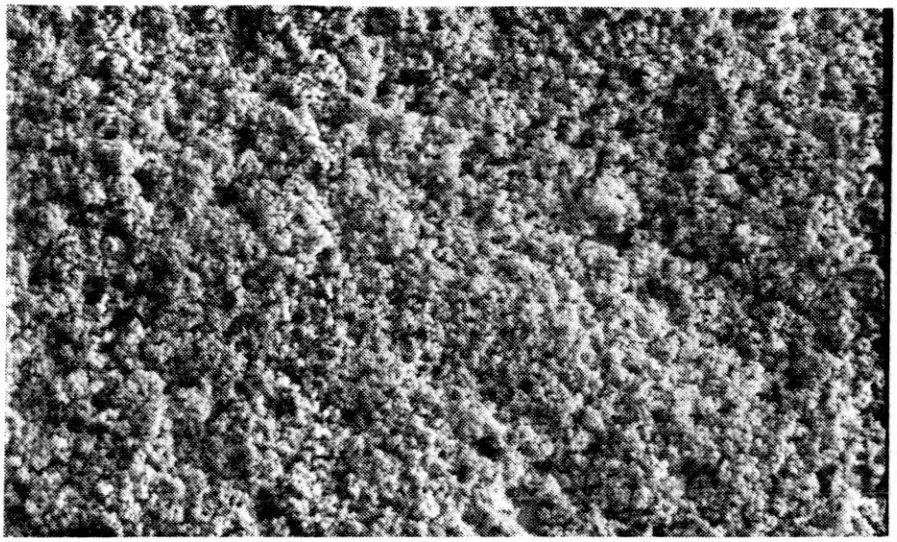

ANATASE 10.0μ

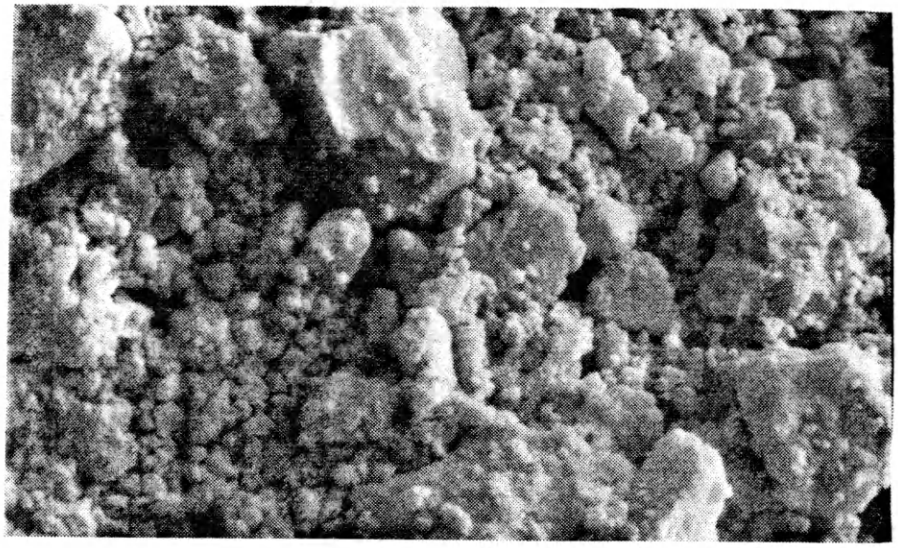

RUTILE 10.0μ

Figure 15 Electron micrographs showing grain sizes of anatase and rutile.

efficiency because only two grain sizes were available, one for anatase and one for rutile, and the uncertainty in these data was too large to warrant such specific considerations.

C. Effect of Doping

1. Results

In Figure 16 the data for doped anatase is presented. There are a relatively small number of points because the amount of n-type doped anatase available was fairly limited. In these data there is also some large scatter at short illumination times. The presence of an induction period here can neither be affirmed nor denied because of a lack of points at short illumination times.

2. Discussion

The proposed model for the small particles of pure rutile and anatase suspended in solution assumes that they have flat bands since the carrier concentration is very low. For doped, n-type anatase, the carrier concentration is high and a band diagram of the type shown in Figure 2 is proposed. For these band energetics the minority carriers (holes) are most easily injected into the solution. This is because the induced electric field in the depletion region opposes electron flow to the solution.

Most systems using n-type semiconductor electrodes have a metal counter-electrode; thus hole injection takes place at the semiconductor surface and electron injection takes place at the metal counter-electrode. In small conducting particles with no second metal phase, there is no counter

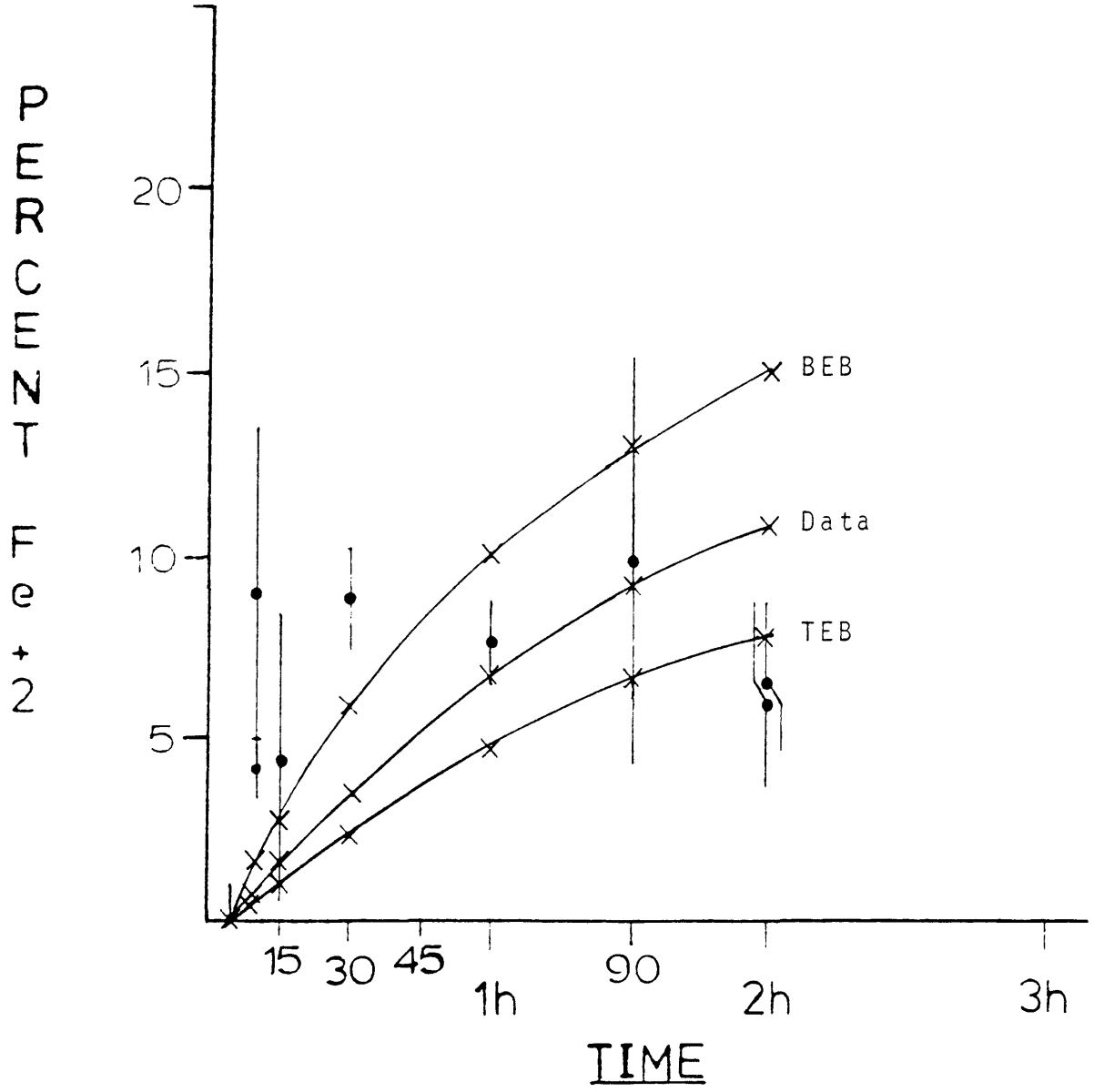

Figure 16

Doped Anatase, overlayed

with Fletcher-Powell fitted curves.

electrode and particles which begin to inject holes into the solution will stop after a brief time since the particles will acquire a negative charge. Also, the electrons must overcome a potential barrier at the interface in order to become injected into the electrolyte. Hence, electron injection from the n-type doped semiconductor powders is expected to be slow.

This type of behavior is consistent with observations for doped anatase. As shown in Table IV, the efficiency of doped anatase is much lower than that for pure anatase. This strongly supports the idea that a depletion region exists in small particles. It is assumed that the photogenerated holes are intercepted by H_2O to produce O_2 for the oxidation reaction.

The calculated curves for the doped anatase are shown in Figure 16. The goodness of fit for these curves was the poorest of all the data. Because of this another type of behavior might be inferred from the data. It is possible that the Fe^{2+} concentration quickly reaches a saturation value (about 10%) and then shows only a minimal increase or even a decrease with time. A plot of the doped anatase data presented in Figure 17 was fitted using this idea of the two kinetic regimes. The initial rate constant (0-30 minutes) was 0.0072, and the final rate constant (30-120 minutes)

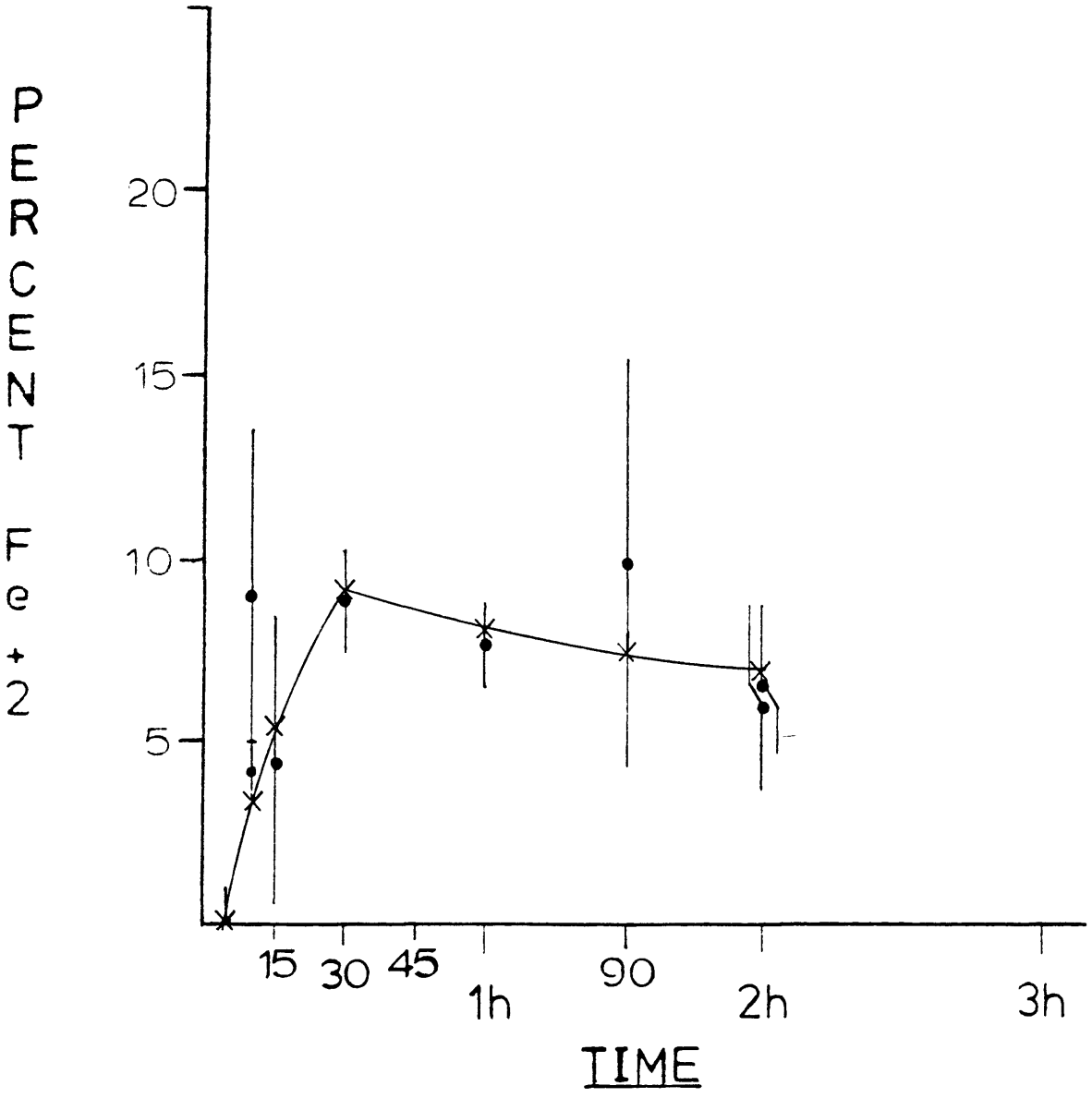

Figure 17

Doped Anatase assuming two rate constants.

Table IV

Comparison of rate constants at x= 9.5

for Doped and pure Anatase

	Doped Anatase	Anatase
TEB	0.0032	0.0076
Data	0.0018	0.0043
BEB	0.0010	0.0021

was -0.0002. This would support the proposal that the particles do indeed acquire a positive charge and this charge inhibits further reduction. However, statistics were not good enough to make definitive selection between the two kinetic models.

D. Effect of Platinization

Figure 18 presents the data for doped anatase onto which platinum had been deposited by photoreduction. Platinized undoped anatase was not available in sufficient quantities to accumulate data for a kinetic run so the effects of platinization were only studied on doped anatase.

As mentioned in section I platinum is a well known catalyst for reduction. Others have clearly shown that the addition of platinum on particles greatly enhances the reduction of H_2O to H_2.[25] Photoreduced platinum does not coat the entire TiO_2 particle; instead it occurs in islands. These "photochemical diodes"[26] provide the electrode and metal counter-electrode system needed for efficient reduction of water, all on the same particle. It is logical to assume that since the Fe^{3+}/Fe^{2+} couple is more positive than the H^+/H_2 couple (see Figure 3), any ferric ion in the vicinity of a photogenerated electron will be preferentially reduced.

Platinum does have a significant effect on the rate constants as shown in Table V. However, the increase in the amount of reduction due to platinization is not as dramatic as is seen by others. For example, Sakata noted that the rate of hydrogen gas evolution from TiO_2 powders increase by a factor of 20 to 100 in the presence of even a small amount

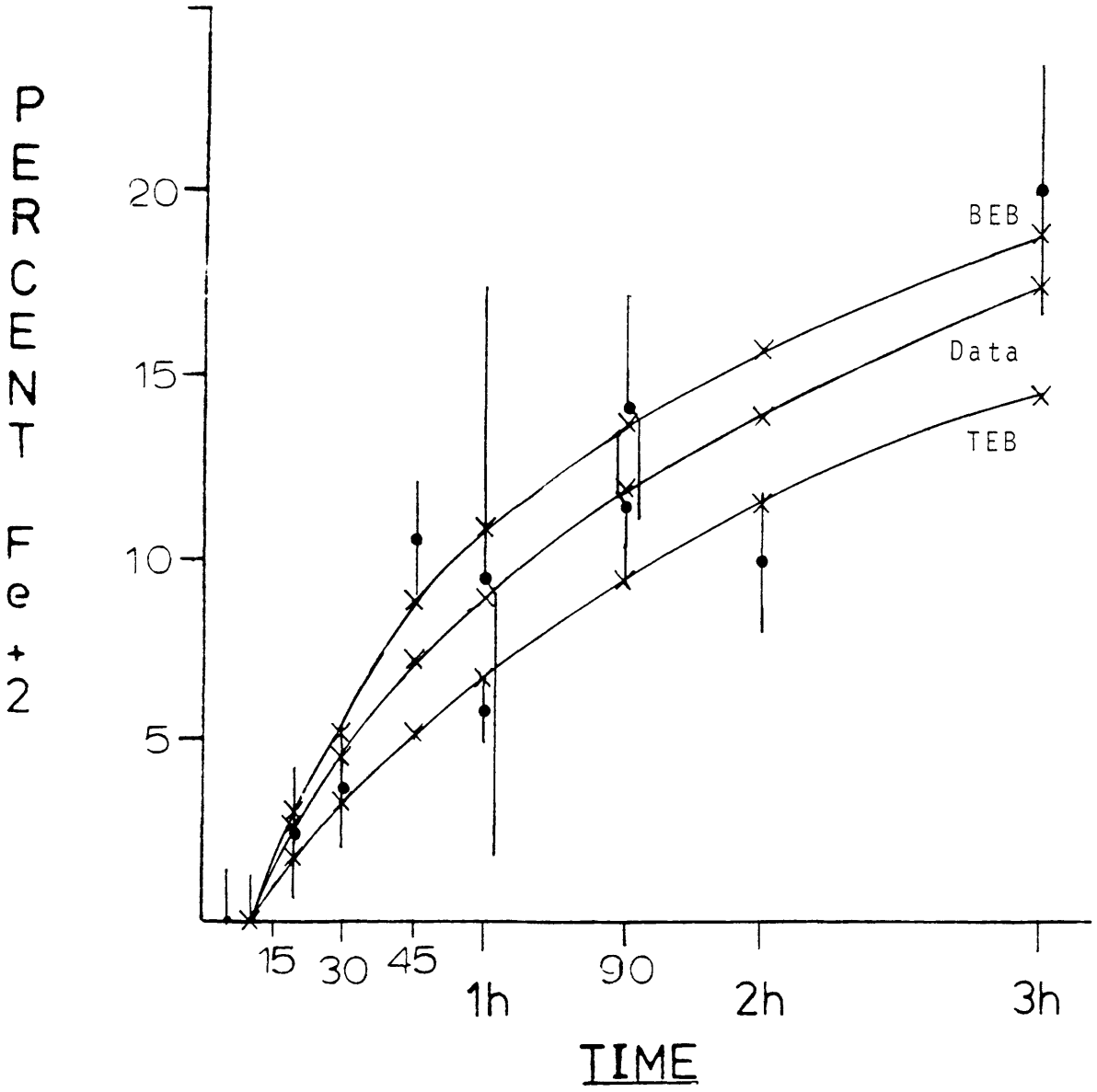

Figure 18

Platinized, Doped Anatase,

overlayed with Fletcher-Powell

fitted curves.

Table V

Comparison of rate constants at x= 9.5

for platinized doped, doped and pure anatase

	Platinized Doped Anat.	Doped Anatase	Anatase
TEB	0.0032	0.0032	0.0076
Data	0.0028	0.0018	0.0043
BEB	0.0019	0.0010	0.0021

of platinum[27]. This is most easily explained by the existance of the barrier to electron transfer in doped anatase. The calculated curves are also shown in Figure 18.

E. Effect of Hole Acceptor

Figure 19 presents the data for anatase in ferric chloride solution to which was added enough sodium acetate to make it 0.014 molar in the acetate ion (CH_3COO^-), which is a good acceptor of holes for oxidation to CO_2. This small amount of sodium acetate did not drastically affect the optical properties of the ferric chloride solution, thus the spectral distribution striking each particle was not altered.

Anatase, in the presence of a hole acceptor should be a much more efficient system for ferric ion reduction compared to the case where anatase is used without a good hole acceptor and this is reflected by the rate constants shown in Table VI. The acetate ion is a sacrificial agent which is very easily oxidized. Its effect on anatase is to scavenge holes before they can back-oxidize the ferrous ion. This results in a higher overall rate constant for the system. The calculated curves are included in Figure 19.

In addition to the affect of a hole acceptor on anatase, its affect on other systems was briefly studied. These results are summarized in Table VII. The hole acceptor generally increased the amount of reduction seen for a particular time of illumination.

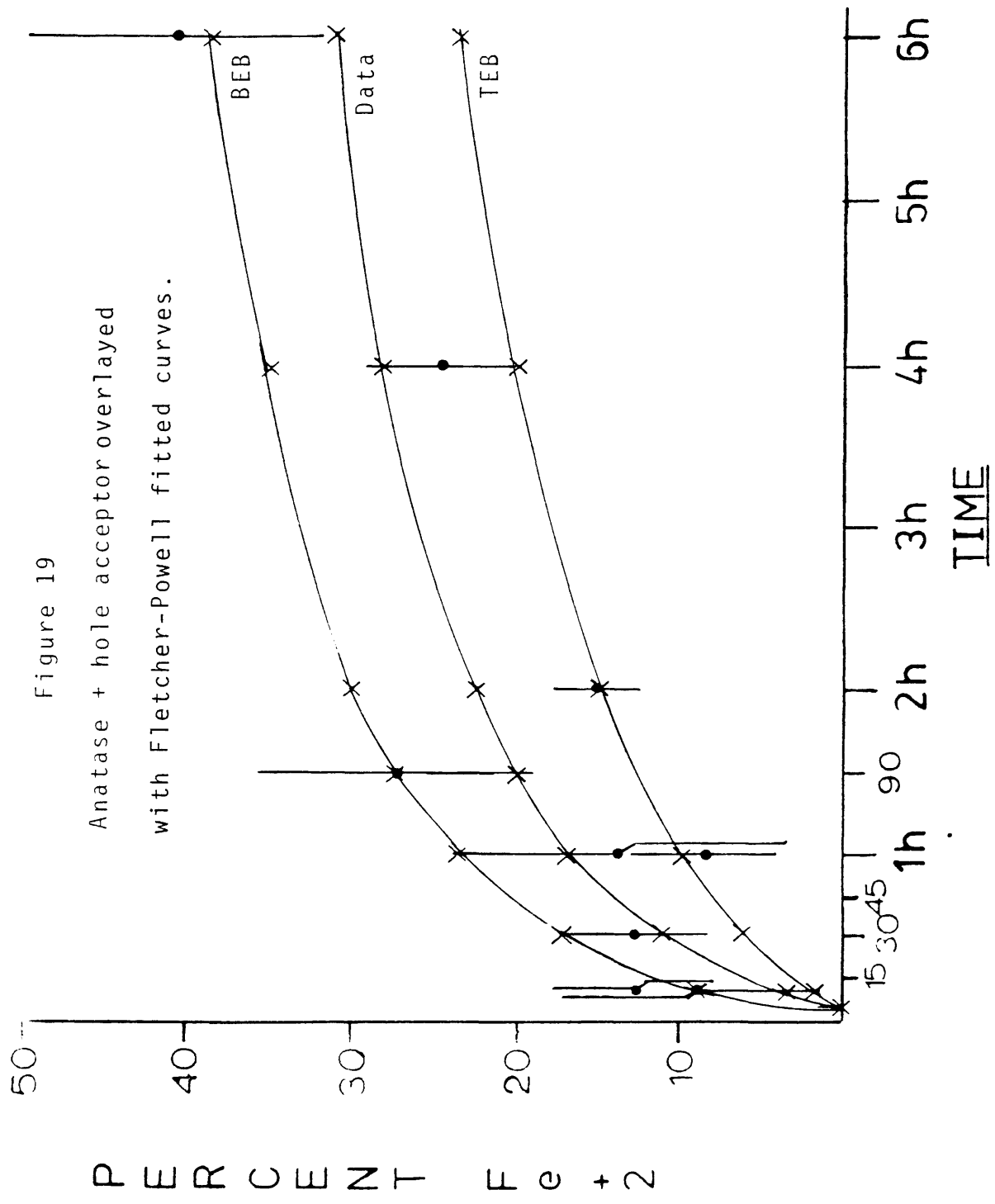

Figure 19

Anatase + hole acceptor overlayed with Fletcher-Powell fitted curves.

Table VI

Effect of hole acceptor on

rate constants at x = 9.5

	Anatase + AC^-	Anatase
TEB	0.0186	0.0076
Data	0.0079	0.0004
BEB	0.0028	0.0021

Table VII

Effect of hole acceptor

on selected semiconductors

Substance	Time	With hole Acceptor	Without Hole Acceptor
Platinized Doped Anatase	10 min.	0.0	0.0
	1 hr.	13.6 ± 2%	5.8 ± .9% 9.7 ± 4%
Platinized Anatase	2 hr.	15.6 ± 3.6%	20.5 ± 10%
	15 min.	11.1 ± 2.5%	
Doped Anatase	1 hr.	10.1 ± 3.2%	7.4 ± 1.6%
Rutile	1 hr.	9.1 ± 1.5%	7.6 ± 1.6%

F. Miscellaneous Effects

Summarized in Table VIII are the results of a breif investigation of the effect of changing the relative amounts of various species in this system. Overall, it can be qualitatively said that small errors in the amount of TiO_2 and concentrations of solution species have little effect on the amount of reduction for a particular length of illumination.

Table VIII

Effect of varying certain concentrations

on normal run amounts of reduction.

Substance	Time	Amount	Normal Amount
-400 mesh Rutile	1 hr.	8.2 ± 1.4%	6.7 ± 1.9%
Anatase 2x Amt. Anat.	1 hr.	10.8 ± 2.5%	18.7 ± 2.5%
Anatase ½ conc $FeCl_3$	1 hr.	14.1 ± 5.5%	18.7 ± 2.5%
Anatase 5x conc HAC^-	1 hr.	18.2 ± 4.5%	18.7 ± 2.5%

V. CONCLUSIONS AND COMMENTS

The rate constants reported here are the first of their kind and because of this, should be viewed as a basis for comparison with future work. These results are summarized in Table IX and certain conclusions can be drawn from them:

1. These data clearly show that the photoconversion process with the anatase powder used in this experiment is more efficient than the rutile. What was not made clear was whether this effect was due to the smaller grain size of anatase or to its more negative conduction band potential, or to some combination of the two effects.

2. It can be clearly stated that n-type, oxygen vacancy doping decreases the system's efficiency. This should be due to the creation of a depletion layer in the particles which inhibits electron injection.

3. Platinization increased the efficiency of electron injection to the ferric ion for this system. This is probably due to its catalytic properties.

4. The addition of a hole acceptor to the solution definately allows the rate of electron injection to increase. This is due to its hole scavenging characteristics, which reduces electron-hole recombination and permits the electron concentration on the particle to build up.

Table IX

Summary of rate constants

for all substance.

Substance	BEB	Data	TEB
Anatase	0.0021	0.0043	0.0076
Rutile	0.0006	0.0012	0.0021
Doped Anatase	0.0010	0.0018	0.0032
Platinized Doped Anatase	0.0019	0.0028	0.0032
Anatase + Hole Acceptor	0.0028	0.0079	0.0186

While much has been learned, further refinement is needed to reduce the experimental uncertainty in these experiments and therefore to allow better definition of the various effects. This could be done by accumulating better statistics in the Mossbauer spectra, and controlling more tightly experimental variables such as sample temperatures and the light intensities. Particularly helpful would be a means of removing or more accurately controlling the broadened Fe^{3+} Mossbauer resonance.

As an extension of this work, the effect of grain size on the efficiency of electron injection needs to be studied more thoroughly. This could be done by measuring rate constants on a series of powders of anatase and rutile with differing grain sizes. This could help answer the question of what controls the difference in efficiencies between anatase and rutile. Kinetic data also needs to be accumulated for doped rutile, platinized anatase and platinized rutile. This would help quantify the effects of these variables and give more specific information on the mechanism of charge transfer in TiO_2.

This mechanism is assumed to be very much like the mechanisms postulated for other oxide semiconductors. Light is obsorbed by the particle and an electron-hole pair is produced. If this pair is produced where an electric field

exists (the space charge region) or near the surface of the semiconductor, it is highly probable that the electron or hole will reach the surface. Once at the surface it can either back-react with its counter-part, be injected into the solution or fall into a surface state, where either of the two aforementioned fates awaits it. Once in solution the reduced species can back-oxidize.

Each step in this process has at least two branches an electron or hole can take. This work studied only the overall probability from light absorption to reduction. More work needs to be done to learn about the individual steps. Answers could be gained by using techniques such as Auger spectroscopy and LEED to tell what solution species are actually adsorbed on the TiO_2 surface. Flash-photolysis could also be used to study the instantaneous production of reduced species on the TiO_2 surface, hence getting information on rates of instantaneous back oxidation of these ions.

Another area where work is badly needed is to relate theoretical microscopic quantum efficiencies with measured rates of reduction of solution species. In the literature there presently exist two broad classes of papers. The first deals with theoretical expressions for quantum efficiencies of semiconductor electrodes under illumination[28-30], while the second is highly qualitative in nature[31-33]. In

the latter, the researcher typically measures the rate of evolution of some reduced species as a function of light intensity, solution species, platinization, etc. There are many variables to consider in a system of particles in solution such as back reactions, turbidity, light absorption by solution species and particle size and shape. But techniques such as flash-photolysis and Mossbauer spectroscopy can be used to unravel parts of the puzzle. This is an exciting area of research which holds much promise for future work.

REFERENCES CITED

1. B. Kraeutler and A. Bard, Jour. Amer. Chem. Soc., 100, 5985, (1978).

2. T. Sakata and T. Kawai, Chem. Phys. Lett., 88, 50, (1982).

3. T. Inoue and A. Fujishima, Nature, 100, 637, (1979).

4. A. Nozik, Appl. Phys. Lett., 30, 567, (1977).

5. A. Henglein, Ber. Bunsenges Phys. Chem., 86, 241, (1982).

6. A. Bard, Science, 207, 140, (1980).

7. J. Bockris, Basic Research Needs and Opportunities on Interfaces in Solar Materials, Conf-8006156, D.O.E., p.72, (1981).

8. A. Nozik, Photovoltaic and Photoelectrochemical Solar Energy Conversion, N.Y., Plenum Press, p.263, (1981).

9. Ibid.

10. L. May, Introduction to the Mossbauer Effect, N.Y., Plenum Press, p.9, (1971).

11. May, Ibid., p.49.

12. May, Ibid., p.107.

13. A. Nozik, PhD thesis, Mossbauer Studies of Ions in Ice, Yale University, p.11, (1967).

14. A Nozik and M. Kaplan, J. Chem. Phys., 49, 4141, (1968).

15. Ibid.

16. H. Wickman and M. Klein, Phys. Rev., 152, 731 (1966).

17. S. Morup and J. Knudsen, J. Chem. Phys., 65, 536, (1979).

18. Ibid.

19. A. Bard, J. Chem. Phys., 61, 82, (1982).

20. A. Nozik, PhD thesis, p.40.

21. Morup, op cit.

22. A. Nozik, PhD thesis, p.27.

23. R. Alberty, Physical Chemistry, John Wiley & Sons, p.479, (1979).

24. A. Frank, Solar Energy Research Institute, personal communication, (1983).

25. B. Kraeutler and A.J. Bard, J. Am. Chem. Soc., 100, 19, (1978).

26. A. Nozik, Appl. Phys. Lett., 30, 11, (1977).

27. T. Sakata, T. Kawai and K. Hashimoto, Chem. Phys. Lett., 88, 1, (1982).

28. R. Wilson, J. Apple. Phys., 48, 10, (1977).

29. M. Hanschuh, W. Lorenz, C. Aegerter and T. Kattle, J. Electroandal Chem., 144, 2, (1983).

30. M. Wrighton and A. Ellis, J. Am. Chem. Soc., 98, 10, (1976).

31. T. Inoue, A. Fujishma, S. Konisi and K. Honda, Nature, 277, (1979).

32. B. Kraeutler and A. Bard, J. Am. Chem. Soc., 99, 23, (1977).

33. B. Kraeutler and A. Bard, J. Am. Chem. Soc., 100, 19, (1978).

APPENDIX I

AREA CORRECTION CALCULATIONS

A. Fe^{3+} Area

In many spectra the computer fitted the broadened Fe^{3+} component with a very broad Lorentzian peak which heavily weights the Fe^{3+}/Fe^{2+} ratio toward Fe^{3+}. See Figure 20. The correct area A_3' is calculated by integrating the broad Lorentzian over the limits of the actual spectra and subtracting the rectangular area above it.

The fitting routine returns a plot of the fitted spectrum overlaying the actual spectrum. It also returns values for the position, width and intensity of each fitted peak. To calculate the correct area (A_3') for the broadened Fe^{3+} peak, the following procedure must be used:

The area of a peak can be calculated from its width at half intensity, and its intensity, I, where $A = \frac{\pi}{2}\Gamma I$, for a Lorentzian.

The computer calculates:

$$I_3,\ \Gamma_3,\ I_2,\ \Gamma_2,\ I_2',\ \Gamma_2',\ I_3',\ \Gamma_3',\ P_3'$$

and $$Fe^{2+} = \frac{I_{2\ 2} + I_{2'\ 2'}}{I_2\Gamma_2 + I_2'\Gamma_2' + I_3\Gamma_3 + A_3'(\frac{2}{\pi})} * 100$$

The correct area for the broadened Fe^{3+} component, A_3', must be computed from spectrum parameters, as

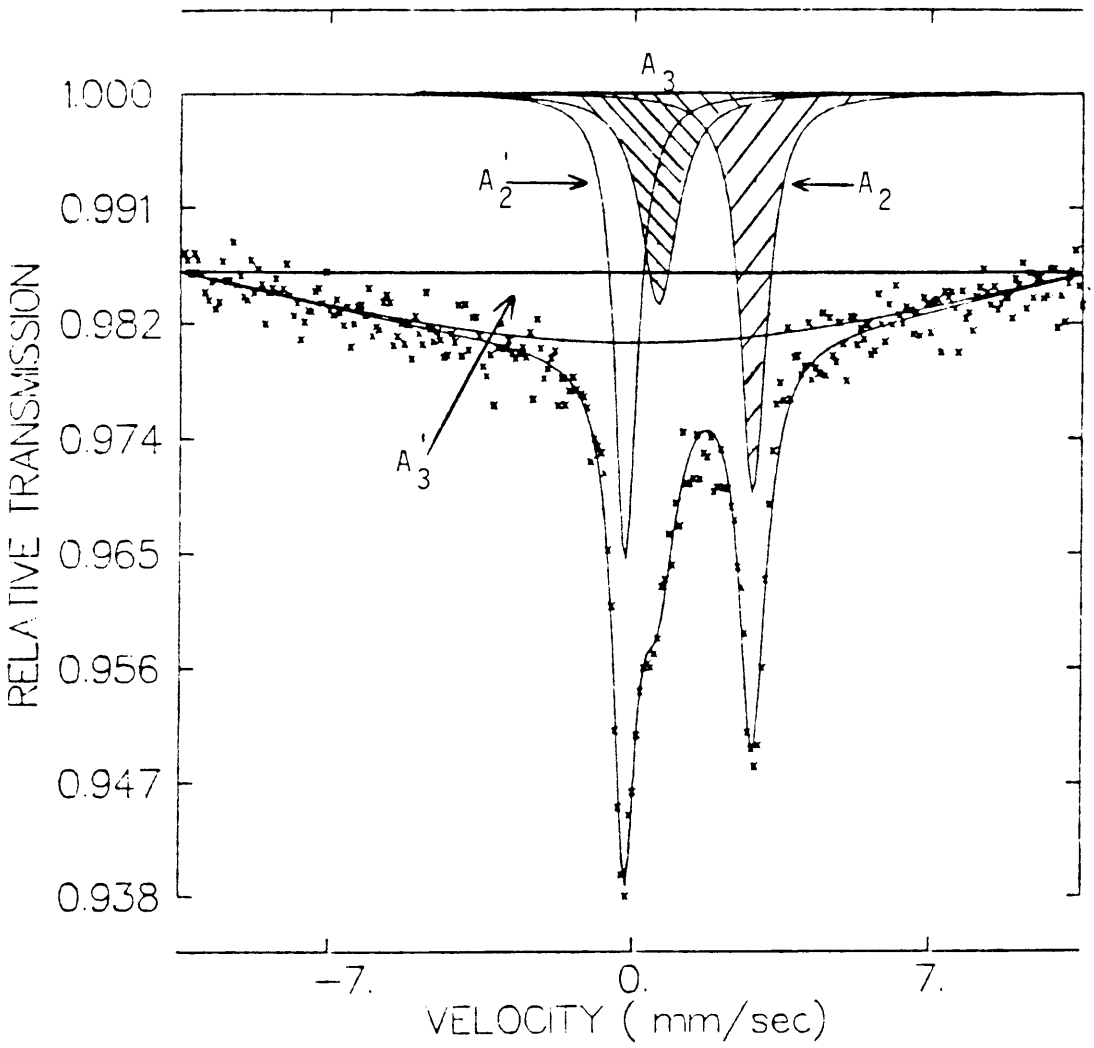

Figure 20

Mossbauer spectrum used as example for Appendix I.

$$A_3' = \int_{1}^{255} \frac{I_3'\, dP}{1 + \{\frac{2(P - P_3')}{\Gamma_3'}\}} - 255I.$$

Let $x = \frac{2(P - P_3')}{\Gamma_3'}$ so $dx = \frac{2\, dP}{\Gamma_3'}$, therefore

$$A_3' = \frac{I_3'\Gamma_3'}{2} \int \frac{dx}{(1+x^2)} - 255\, I_3'/\{1 + \{\frac{2(1-P_3')}{\Gamma_3'}\}^2\}.$$

After integration,

$$A_3' = \frac{\Gamma_3'I_3'}{2} \{\mathrm{Tan}^{-1} \frac{2(255-P_3')}{\Gamma_3'} - \mathrm{Tan}^{-1} \frac{2(1-P_3')}{\Gamma_3'}\}$$

$$- 255\, I_3'/\{1 + \{\frac{2(1-P_3')}{\Gamma_3'}\}^2\}.$$

B. Fe^{2+} Area

It is assumed that the ferrous ion in ice gives a quadrupole pair for its absorbtion spectrum. In some spectra the lower velocity ferrous peak, Fe^{2+} is unresolved from the narrow ferric peak, Fe^{3+}_s. When the lower velocity Fe^{2+} peak, Fe^{2+}_-, cannot be resolved from Fe^{3+}_s it is assumed to have the same area as the higher velocity Fe^{2+} peak, Fe^{2+}_+. The area of Fe^{2+}_- is then subtracted from Fe^{3+}_s which conserves total area. It is then possible to calculate the ferric/ferrous ratio. The total area is then:

$(Fe^{3+}_{b}) + (Fe^{3+}_{s}) + (Fe^{2+}_{-}) + (Fe^{2+}_{+})$ = Total Area = TA

where () indicates the area of that peak.

$\%Fe^{2+} = \{(Fe^{2+}_{-}) + (Fe^{2+}_{+})\}/TA * 100$

APPENDIX II - SPECTRUM PARAMETERS

KEY

(spectrum number and information)

p	w	A	
Fe^{+3}_{B}			broadened Fe^{+3} peak
Fe^{+3}_{S}			sharp Fe^{+3} peak
Fe^{+2}_{-}			lower velocity Fe^{+2} peak
Fe^{+2}_{+}			higher velocity Fe^{+2} peak

List of abbreviations:

p - position of peak (mm/sec), relative to zero of velocity.

w - width of peak (mm/sec)

a - area of peak (counts * mm/sec)

Anat. - anatase

Rut. - rutile

HAc - hole acceptor

Pt - platinized

D - doped (n-typed)

CC - computer calculated and width not involved

CNC - concentration

APPENDIX II - SPECTRUM PARAMETERS

	p	w	A
1559 Anatase - 2 min.			
Fe^{3+}_B	.63	4.53	.41
Fe^{3+}_S	.50	.76	.39
Fe^{2+}_-	-	-	-
Fe^{2+}_+	-	-	-
< 2.7% Fe^{2+}			.80
1561 Anatase - 5 min.			
Fe^{3+}_B	.71	5.35	.30
Fe^{3+}_S	.48	.98	.51
Fe^{2+}_-	-	-	-
Fe^{2+}_+	-	-	-
Fe^{2+} of ≤ .88%			.81
1564 Anatase - 10 min.			
Fe^{3+}_B	.92	4.94	.44
Fe^{3+}_S	.47	.66	.33
Fe^{2+}_-	-	-	-
Fe^{2+}_+	-	-	-
≤ 2% Fe^{2+}			.77
1571 Anatase - 15 min.			
Fe^{3+}_B	1.15	CC	.38
Fe^{3+}_S	.15	.65	.43
Fe^{2+}_-	-	-	-
Fe^{2+}_+	-	-	-
≤ 2% Fe^{2+}			.81
1565 Anatase - 20 min.			
Fe^{3+}_B	.96	4.94	.51
Fe^{3+}_S	.44	.86	.25
Fe^{2+}_-	-.08	.48	.02
Fe^{2+}_+	2.84	.48	.02
5.9 ± 3.2%			.80
1566 Anatase - 30 min.			
Fe^{3+}_B	1.29	4.12	.38
Fe^{3+}_S	.30	1.15	.24
Fe^{2+}_-	-.08	.33	.05
Fe^{2+}_+	2.88	.33	.05
9.4 ± 2.7%			.72

APPENDIX II - SPECTRUM PARAMETERS (continued)

	p	w	A
1569 Anatase - 45 min.			
Fe^{3+}_{B}	.52	CC	.36
Fe^{3+}_{S}	.48	.70	.40
Fe^{2+}_{-}	-.24	.71	.03
Fe^{2+}_{+}	2.82	.71	.03
12.2 ± 2.2%			.82
1691 Anatase - 1 hour			
Fe^{3+}_{B}	-	-	-
Fe^{3+}_{S}	.42	.70	.54
Fe^{2+}_{-}	-.10	.32	.06
Fe^{2+}_{+}	2.79	.32	.06
18.7 ± 2.5%			.66
1570 Anatase - 90 min.			
Fe^{3+}_{B}	.42	CC	.25
Fe^{3+}_{S}	.51	.74	.49
Fe^{2+}_{-}	-.23	.30	.08
Fe^{2+}_{+}	2.87	.30	.08
14.5 ± 3.1%			.90

	p	w	A
1663 Anatase - 1 hour			
Fe^{3+}_{B}	.56	5.65	.28
Fe^{3+}_{S}	.51	.60	.54
Fe^{2+}_{-}	-.17	.47	.08
Fe^{2+}_{+}	2.80	.34	.08
16.9 ± 3.5%			.98
1572 Anatase - 75 min.			
Fe^{3+}_{B}	.51	CC	.46
Fe^{3+}_{S}	.42	.89	.39
Fe^{2+}_{-}	-.09	.48	.05
Fe^{2+}_{+}	2.93	.48	.05
16.1 ± 4.5%			.95
1634 Anatase - 90 min.			
Fe^{3+}_{B}	.54	CC	.28
Fe^{3+}_{S}	.47	.77	.28
Fe^{2+}_{-}	-.21	.25	.07
Fe^{2+}_{+}	2.83	.29	.07
20.1 ± 3.0%			.70

APPENDIX II - SPECTRUM PARAMETERS (continued)

	p	w	A
1735 Anatase - 90 min.			
Fe^{3+}_{B}	.47	CC	.20
Fe^{3+}_{S}	.54	.53	.40
Fe^{2+}_{-}	-.49	.44	.05
Fe^{2+}_{+}	2.77	.32	.05
14.5 ± 9.4%			.70

	p	w	A
1643 Anatase - 2 hours			
Fe^{3+}_{B}	.23	5.35	.10
Fe^{3+}_{S}	.43	.73	.41
Fe^{2+}_{-}	-.10	.27	.07
Fe^{2+}_{+}	2.84	.27	.07
13.2 ± 10.0%			1.09

	p	w	A
1703 Anatase - 2 hours			
Fe^{3+}_{B}	.44	CC	.44
Fe^{3+}_{S}	.56	.58	.32
Fe^{2+}_{-}	-.18	.42	.06
Fe^{2+}_{+}	2.78	.37	.06
14.9 ± 2.4%			.88

	p	w	A
1694 Anatase - 3 hours			
Fe^{3+}_{B}	.38	5.35	.10
Fe^{3+}_{S}	.60	.75	.41
Fe^{2+}_{-}	-.10	.36	.07
Fe^{2+}_{+}	2.81	.36	.07
21.9 ± 10.4%			.68

	p	w	A
1702 Anatase - 4 hours			
Fe^{3+}_{B}	.21	CC	.30
Fe^{3+}_{S}	.53	.70	.33
Fe^{2+}_{-}	-.21	.31	.05
Fe^{2+}_{+}	2.87	.25	.75
14.3 ± 2.4%			1.43

	p	w	A
1695 Anatase - 5 hours			
Fe^{3+}_{B}	.36	CC	.18
Fe^{3+}_{S}	.19	.98	.53
Fe^{2+}_{-}	-.10	.38	.09
Fe^{2+}_{+}	2.85	.38	.09
20.2 ± 13.6%			.89

APPENDIX II - SPECTRUM PARAMETERS (continued)

	p	w	A
1700 Anatase - 6 hours			
Fe^{3+}_{B}	.54	CC	.24
Fe^{3+}_{S}	.10	.52	.57
Fe^{2+}_{-}	-.15	.31	.14
Fe^{2+}_{+}	2.77	.26	.14
25.5 ± 8.2%			1.09
1621 Rutile - 10 min.			
Fe^{3+}_{B}	.52	5.35	.49
Fe^{3+}_{S}	.48	.65	.46
Fe^{2+}_{-}	-.08	.24	.02
Fe^{2+}_{+}	2.80	.24	.02
3.9 ± 2.7%			.99
1574 Rutile - 25 min.			
Fe^{3+}_{B}	.71	6.89	.46
Fe^{3+}_{S}	.44	.75	.50
Fe^{2+}_{-}	-.08	.29	.03
Fe^{2+}_{+}	2.89	.29	.03
6.8 ± 0.9%			1.02

	p	w	A
1573 Rutile - 5 min.			
Fe^{3+}_{B}	.53	3.13	.60
Fe^{3+}_{S}	.49	.67	.38
Fe^{2+}_{-}	-	-	-
Fe^{2+}_{+}	-	-	-
≤ 1.4% of Fe^{2+}			.98
1608 Rutile - 15 min.			
Fe^{3+}_{B}	.74	5.36	*
Fe^{3+}_{S}	.49	.73	*
Fe^{2+}_{-}	-.08	.33	*
Fe^{2+}_{+}	2.72	.33	*
1.8 ± 1.8%			
1722 Rutile - 30 min.			
Fe^{3+}_{B}	.68	CC	.35
Fe^{3+}_{S}	.47	.58	.40
Fe^{2+}_{-}	-	-	-
Fe^{2+}_{+}	-	-	-
≤ 2.0 Fe^{2+}			.75

* - irregular sample

APPENDIX II - SPECTRUM PARAMETERS (continued)

	p	w	A
1577 Rutile - 35 min.			
Fe^{3+}_{B}	.55	.68	.38
Fe^{3+}_{S}	.45	.72	.52
Fe^{2+}_{-}	-.08	.23	.02
Fe^{2+}_{+}	2.84	.23	.02
5.2 ± 0.9%			.94
1720 Rutile - 45 min.			
Fe^{3+}_{B}	.51	4.10	.60
Fe^{3+}_{S}	.48	.67	.60
Fe^{2+}_{-}	-.08	.22	.01
Fe^{2+}_{+}	2.88	.22	.01
3.0 ± 0.6%			1.21
1579 Rutile - 75 min.			
Fe^{3+}_{B}	.08	5.35	.45
Fe^{3+}_{S}	.45	.80	.36
Fe^{2+}_{-}	-.08	.53	.02
Fe^{2+}_{+}	2.50	.53	.02
6.7 ± 1.4%			.85

	p	w	A
1575 Rutile - 45 min.			
Fe^{3+}_{B}	.66	CC	.38
Fe^{3+}_{S}	.48	.62	.51
Fe^{2+}_{-}	-.10	.21	.01
Fe^{2+}_{+}	2.82	.21	.01
2.6 ± 0.5%			.91
1578 Rutile - 1 hour			
Fe^{3+}_{B}	.83	CC	.32
Fe^{3+}_{S}	.44	1.03	.50
Fe^{2+}_{-}	-.08	.39	.02
Fe^{2+}_{+}	2.91	.39	.02
6.7 ± 1.9%			.86
1576 Rutile - 90 min.			
Fe^{3+}_{B}	1.20	CC	.24
Fe^{3+}_{S}	.42	.84	.43
Fe^{2+}_{-}	.08	.29	.02
Fe^{2+}_{+}	2.88	.29	.02
7.2 ± 2.1%			.71

APPENDIX II - SPECTRUM PARAMETERS (continued)

	p	w	A
1620 Rutile - 105 min.			
Fe^{3+}_{B}	.46	5.35	.25
Fe^{3+}_{S}	.94	.84	.63
Fe^{2+}_{-}	-.08	.62	.03
Fe^{2+}_{+}	2.97	.62	.03
6.3 ± 5.6%			.94
1716 Rutile - 3 hours			
Fe^{3+}_{B}	.53	CC	.22
Fe^{3+}_{S}	.45	.62	.41
Fe^{2+}_{-}	-.10	.42	.03
Fe^{2+}_{+}	2.77	.42	.03
9.3 ± 2.0%			.69
1719 Rutile - 5 hours			
Fe^{3+}_{B}	-	-	-
Fe^{3+}_{S}	.49	.60	.61
Fe^{2+}_{-}	-.10	.43	.06
Fe^{2+}_{+}	2.87	.43	.06
16.5 ± 14.5%			.73

	p	w	A
1580 Rutile - 2 hours			
Fe^{3+}_{B}	.93	5.35	.27
Fe^{3+}_{S}	.44	.86	.32
Fe^{2+}_{-}	-.08	.33	.02
Fe^{2+}_{+}	2.83	.37	.02
7.6 ± 1.6%			.63
1728 Rutile - 4 hours			
Fe^{3+}_{B}	.26	CC	.50
Fe^{3+}_{S}	.49	.59	.50
Fe^{2+}_{-}	-.19	.18	.05
Fe^{2+}_{+}	2.81	.25	.05
10.9 ± 1.9%			1.10
1723 Rutile - 6 hours			
Fe^{3+}_{B}	-	-	-
Fe^{3+}_{S}	.62	.85	.51
Fe^{2+}_{-}	-.10	.32	.05
Fe^{2+}_{+}	2.85	.32	.05
17.3 ± 0.5%			.61

APPENDIX II - SPECTRUM PARAMETERS (continued)

	p	w	A
1725 Anat. + HAc - 5 min.			
Fe^{3+}_{B}	.79	CC	.42
Fe^{3+}_{S}	.47	.72	.31
Fe^{2+}_{-}	-	-	-
Fe^{2+}_{+}	-	-	-
< 1.5% Fe^{2+}			.73
1716 Anat. + HAc - 10 min.			
Fe^{3+}_{B}	.56	CC	.48
Fe^{3+}_{S}	.54	.34	.28
Fe^{2+}_{-}	-.17	.34	.05
Fe^{2+}_{+}	2.79	.32	.05
13.2 ± 4.9%			.76
1730 Anat. + HAc - 10 min.			
Fe^{3+}_{B}	.38	CC	.35
Fe^{3+}_{S}	.56	.72	.33
Fe^{2+}_{-}	-.09	.51	.03
Fe^{2+}_{+}	2.84	.42	.03
9.5 ± 9.4%			.74
1724 Anat. + HAc - 30 min.			
Fe^{3+}_{B}	.38	CC	.41
Fe^{3+}_{S}	.58	.97	.28
Fe^{2+}_{-}	-.11	.45	.03
Fe^{2+}_{+}	2.79	.29	.03
13.0 ± 4.3%			.75
1643 Anat. + HAc - 1 hour			
Fe^{3+}_{B}	.47	5.65	.28
Fe^{3+}_{S}	.53	.09	.33
Fe^{2+}_{-}	-.18	.59	.05
Fe^{2+}_{+}	2.85	.34	.05
14.0 ± 10.5%			.71
1704 Anat. + HAc - 1 hour			
Fe^{3+}_{B}	.52	5.35	.35
Fe^{3+}_{S}	.58	.83	.30
Fe^{2+}_{-}	-.21	.44	.06
Fe^{2+}_{+}	2.83	.25	.03
8.9 ± 4.6%			.74

APPENDIX II - SPECTRUM PARAMETERS (continued)

	p	w	A
1708 Anat. + HAc - 90 min.			
Fe^{3+}_{B}	.25	CC	.29
Fe^{3+}_{S}	.54	.79	.13
Fe^{2+}_{-}	-.19	.30	.08
Fe^{2+}_{+}	2.82	.41	.08
28.0 ± 8.4%			.58

	p	w	A
1721 Anat. + HAc - 2 hours			
Fe^{3+}_{B}	.34	CC	.23
Fe^{3+}_{S}	.45	.79	.32
Fe^{2+}_{-}	-.25	.19	.07
Fe^{2+}_{+}	2.83	.27	.07
15.8 ± 2.7%			.69

	p	w	A
1709 Anat. + HAc - 4 hours			
Fe^{3+}_{B}	.57	CC	.30
Fe^{3+}_{S}	.47	.67	.44
Fe^{2+}_{-}	-.21	.23	.12
Fe^{2+}_{+}	2.84	.27	.12
24.9 ± 4.2%			.98

	p	w	A
1715 Anat. + HAc - 6 hours			
Fe^{3+}_{B}	.14	CC	.28
Fe^{3+}_{S}	.56	.51	.10
Fe^{2+}_{-}	-.18	.31	.13
Fe^{2+}_{+}	2.81	.37	.13
41.5 ± 11.6%			.64

	p	w	A
1675 Doped Anat. - 5 min.			
Fe^{3+}_{B}	.40	CC	.35
Fe^{3+}_{S}	.38	.71	.36
Fe^{2+}_{-}	-	-	-
Fe^{2+}_{+}	-	-	-
≤ 1.0% Fe^{2+}			.71

	p	w	A
1664 Doped Anat. - 10 min.			
Fe^{3+}_{B}	.45	5.65	.20
Fe^{3+}_{S}	.39	.70	.24
Fe^{2+}_{-}	-.10	.31	.02
Fe^{2+}_{+}	2.81	.31	.02
9.3 ± 4.5%			.48

APPENDIX II - SPECTRUM PARAMETERS (continued)

	p	w	A
1731 Doped Anat. - 10 min.			
Fe^{3+}_B	.46	CC	.30
Fe^{3+}_S	.47	.62	.48
Fe^{2+}_-	-.10	.27	.01
Fe^{2+}_+	2.79	.27	.01
3.6 ± 1.1%			.80

	p	w	A
1654 Doped Anat. - 15 min.			
Fe^{3+}_B	.67	CC	.50
Fe^{3+}_S	.45	.69	.42
Fe^{2+}_-	-.10	.28	.02
Fe^{2+}_+	2.84	.28	.02
4.6 ± 4%			.96

	p	w	A
1655 Doped Anat. - 30 min.			
Fe^{3+}_B	.77	CC	.39
Fe^{3+}_S	.42	.72	.51
Fe^{2+}_-	-.10	.31	.04
Fe^{2+}_+	2.85	.31	.04
9 ± 1.5%			.98

	p	w	A
1660 Doped Anat. - 1 hour			
Fe^{3+}_B	.69	CC	.27
Fe^{3+}_S	.44	.76	.67
Fe^{2+}_-	-.10	.31	.04
Fe^{2+}_+	2.84	.31	.04
7.8 ± 1.2%			.92

	p	w	A
1661 Doped Anat. - 90 min.			
Fe^{3+}_B	-	-	-
Fe^{3+}_S	.39	.82	.56
Fe^{2+}_-	-.10	.33	.06
Fe^{2+}_+	2.81	.30	.06
10.2 ± 5.6%			.68

	p	w	A
1734 Doped Anat. - 2 hours			
Fe^{3+}_B	.59	3.18	.54
Fe^{3+}_S	.49	.60	.38
Fe^{2+}_-	.25	.27	.03
Fe^{2+}_+	2.87	.21	.03
6.9 ± 2.1%			.98

APPENDIX II - SPECTRUM PARAMETERS (continued)

	p	w	A
1642 Doped Anat. - 2 hours			
Fe^{3+}_{B}	.21	5.35	.25
Fe^{3+}_{S}	.48	.74	.54
Fe^{2+}_{-}	-.10	.34	.03
Fe^{2+}_{+}	2.90	.34	.03
7.4 ± 1.6%			.85
1623 Pt Doped Anat. - 5 min.			
Fe^{3+}_{B}	.83	5.35	.42
Fe^{3+}_{S}	.43	.59	.46
Fe^{2+}_{-}	-	-	-
Fe^{2+}_{+}	-	-	-
≤ 1.5% Fe^{2+}			.88
1626 Pt Doped Anat. - 10 min.			
Fe^{3+}_{B}	.30	CC	.37
Fe^{3+}_{S}	.41	.63	.42
Fe^{2+}_{-}	-	-	-
Fe^{2+}_{+}	-	-	-
≤ 1.3% Fe^{2+}			.79
1627 Pt Doped Anat. - 20 min.			
Fe^{3+}_{B}	.33	3.70	*
Fe^{3+}_{S}	.47	.79	*
Fe^{2+}_{-}	-.08	.18	*
Fe^{2+}_{+}	3.10	.18	*
2.4 ± 1.8%			
1629 Pt Doped Anat. - 30 min.			
Fe^{3+}_{B}	.65	5.35	.44
Fe^{3+}_{S}	.50	.63	.48
Fe^{2+}_{-}	-.26	.28	.01
Fe^{2+}_{+}	2.83	.28	.01
3.8 ± 1.8%			.94
1630 Pt Doped Anat. - 45 min.			
Fe^{3+}_{B}	.41	5.35	.40
Fe^{3+}_{S}	.49	.62	.32
Fe^{2+}_{-}	-.10	.33	.04
Fe^{2+}_{+}	2.53	.33	.04
10.8 ± 1.5%			.80

* - sample melted

APPENDIX II - SPECTRUM PARAMETERS (continued)

	p	w	A
1638 Pt Doped Anat. - 1 hour			
Fe^{3+}_{B}	.44	5.44	.31
Fe^{3+}_{S}	.46	.71	.55
Fe^{2+}_{-}	-.08	.20	.02
Fe^{2+}_{+}	2.82	.20	.02
5.9 ± 0.9%			.90

	p	w	A
1624 Pt Doped Anat. - 1 hour			
Fe^{3+}_{B}	.60	CC	.26
Fe^{3+}_{S}	.41	.92	.66
Fe^{2+}_{-}	-.10	.28	.05
Fe^{2+}_{+}	2.86	.28	.05
9.7 ± 9%			1.02

	p	w	A
1628 Pt Doped Anat. - 90 min.			
Fe^{3+}_{B}	.28	5.60	.31
Fe^{3+}_{S}	.56	.61	.33
Fe^{2+}_{-}	-.14	.45	.03
Fe^{2+}_{+}	2.77	.45	.03
14.5 ± 3.1%			.70

	p	w	A
1732 Pt Doped Anat. - 90 min.			
Fe^{3+}_{B}	.52	3.21	.40
Fe^{3+}_{S}	.50	.56	.30
Fe^{2+}_{-}	-.21	.26	.04
Fe^{2+}_{+}	2.83	.26	.04
11.7 ± 2.0%			.78

	p	w	A
1625 Pt Doped Anat. - 2 hours			
Fe^{3+}_{B}	.26	5.36	.24
Fe^{3+}_{S}	.44	.77	.55
Fe^{2+}_{-}	-.08	.27	.04
Fe^{2+}_{+}	2.88	.27	.04
10.2 ± 1.9%			.87

	p	w	A
1736 Pt Doped Anat - 3 hours			
Fe^{3+}_{B}	.18	CC	.22
Fe^{3+}_{B}	.50	.65	.30
Fe^{2+}_{-}	-.20	.27	.07
Fe^{2+}_{+}	2.86	.28	.07
20.6 ± 3.4%			.66

APPENDIX II - SPECTRUM PARAMETERS (continued)

	p	w	A
1641 Pt D Anat + HAc - 10 min			
Fe^{3+}_{B}	.54	CC	.41
Fe^{3+}_{S}	.41	.70	.37
Fe^{2+}_{-}	-	-	-
Fe^{2+}_{+}	-	-	-
No Fe^{2+}	present		.78
1640 Pt D Anat + HAc - 1 hr			
Fe^{3+}_{B}	.48	5.35	.31
Fe^{3+}_{S}	.44	.93	.33
Fe^{2+}_{-}	-.12	.29	.05
Fe^{2+}_{+}	2.83	.29	.05
13.6 ± 2.0%			.74
1645 Pt Anat + HAc - 15 min			
Fe^{3+}_{B}	.91	5.65	.19
Fe^{3+}_{S}	.37	1.17	.44
Fe^{2+}_{-}	-.10	.32	.03
Fe^{2+}_{+}	2.85	.32	.03
11.1 ± 3.6%			.69
1646 Pt Anat + HAc - 2 hrs			
Fe^{3+}_{B}	.62	CC	.27
Fe^{3+}_{S}	.38	.97	.28
Fe^{2+}_{-}	-.10	.31	.03
Fe^{2+}_{+}	2.88	.31	.03
11.2 ± 10.0%			.61
1644 D Anat + HAc - 2 hrs.			
Fe^{3+}_{B}	1.20	CC	.24
Fe^{3+}_{S}	.41	1.12	.41
Fe^{2+}_{-}	-.10	.45	.03
Fe^{2+}_{+}	2.90	.45	.03
10.1 ± 3.2%			.91
1647 Rutile + HAc - 2 hrs.			
Fe^{3+}_{B}	.58	CC	.34
Fe^{3+}_{S}	.42	.86	.34
Fe^{2+}_{-}	-.10	.55	.03
Fe^{2+}_{+}	2.75	.55	.03
10.3 ± 1.5%			.74

APPENDIX II - SPECTRUM PARAMETERS (continued)

	p	w	A
1733 Anat 40 mg - 1 hour			
Fe^{3+}_{B}	.56	CC	.24
Fe^{3+}_{S}	.55	.54	.19
Fe^{2+}_{-}	-.18	.33	.02
Fe^{2+}_{+}	2.83	.20	.02
10.8 ± 2.5%			.48

	p	w	A
N1622 -400 Rutile - 1 hr			
Fe^{3+}_{B}	.41	CC	.36
Fe^{3+}_{S}	.42	.86	.43
Fe^{2+}_{-}	-.08	.34	.03
Fe^{2+}_{+}	2.83	.34	.03
8.2 ± 1.4%			.87

	p	w	A
1705 Anat 1/2 conc FeCl 1 hr			
Fe^{3+}_{B}	.64	CC	.32
Fe^{3+}_{S}	.48	.71	.39
Fe^{2+}_{-}	.01	.63	.07
Fe^{2+}_{+}	2.78	.36	.05
14.1 ± 10.1%			.74

	p	w	A
1706 Anat + 5 x HAc - 1 hr			
Fe^{3+}_{B}	.44	CC	.46
Fe^{3+}_{S}	.60	.67	.20
Fe^{2+}_{-}	-.17	.42	.07
Fe^{2+}_{+}	2.81	.40	.07
18.2 ± 4.6%			.81

	p	w	A
1648 Pt Anat - 2 hours			
Fe^{3+}_{B}	.19	5.85	.24
Fe^{3+}_{S}	.39	.98	.35
Fe^{2+}_{-}	-.08	.44	.07
Fe^{2+}_{+}	2.83	.39	.07
20.5 ± 11.2%			.74

	p	w	A
1637 Repeat of Spectrum 1630			
Fe^{3+}_{B}	.53	CC	.63
Fe^{3+}_{S}	.52	.79	.54
Fe^{2+}_{-}	-.24	.30	.18
Fe^{2+}_{+}	2.88	.18	.18
4.0 ± 1.9%			1.33